

APPLICATION OF UV RAMAN SCATTERING TO NON-TRADITIONAL STAND-OFF
CHEMICAL DETECTION

Arthur J. Sedlacek, III[§] and Ming Wu
Atmospheric Sciences Division
Brookhaven National Laboratory
Upton, NY 11973-5000

August 2002

Submitted for publication in
Trends in Applied Spectroscopy

[§] To whom correspondence should be addressed. sedlacek@bnl.gov

By acceptance of this article, the publisher and/or recipient acknowledges the U.S. Government's right to retain a nonexclusive, royalty-free license in and to any copyright covering this paper.

Research by BNL investigators was performed under the auspices of the U.S. Department of Energy under Contract No. DE-AC02-98CH10886.

Application of UV Raman Scattering to Non-Traditional Stand-off Chemical Detection

Arthur J. Sedlacek, III[§] and Ming Wu

Environmental Sciences Department

Brookhaven National Laboratory

Upton, New York 11973

U.S.A.

Abstract:

Today's Hazardous Materials (Haz/Mat) professionals and First Responders (fire and police) increasingly have to confront ever more hazardous and potentially deadly chemical spills and unknown chemical substances as a course of their daily activities. These activities typically require ascertaining the unknown substances' identity followed by the institution of appropriate remediation activities and safety measures as commensurate with the toxicity of the substance. While most of these activities are of a routine nature, the increased daring of terrorists along with their increased access to chemical, biological and, in some cases, nuclear and radiological materials, has increased both the complexity and the hazards confronting these professionals. In light of the fact that the current generation of chemical sensors available to these First Responders require either sample acquisition (followed by sample preparation) or bringing the detector/sensor in close proximity to the unknown spill prior to knowing the identity of the substance in question, we decided to evaluate the efficacy of short-range Raman lidar (Light Detection and Ranging) towards the detection/identification of ground contamination.

The following article provides a review of this "non-traditional" application of Raman lidar to the detection and identification of solid ground contamination and liquid chemical spills. A historical summary of the Raman lidar technique along with an introduction of Raman spectroscopy will be presented, and Raman spectra of CCl₄ and C₂Cl₄ will be used as examples to illustrate pre-resonance and resonance effects. This is then followed by examples of two Raman lidar sensor platforms deployed for this "non-traditional" scenario along with the data acquisition techniques and experimental results.

Keywords:

Raman lidar, Raman spectroscopy, Mini-Raman Lidar System, Standoff detection, *In situ* detection, ground contamination, chemical spills.

[§] To whom correspondence should be addressed. sedlacek@bnl.gov

Introduction

Currently when “First Responders” (*i.e.*, hazardous materials (Haz/Mat) professionals, fireman, policemen) come into contact with an unknown chemical spill, the present-day chemical sensor suite available to these professionals require either that the sensor itself be brought into close proximity to the unknown spill (<1 ft.) or that a small sample of the substance be collected for instrumental analysis onboard a mobile laboratory. Examples of these types of sensors include: continuous air monitoring (CAM) sensors based on ion mobility; surface acoustic wave (SAW) sensors; Drager tubes, (which can detect vapors in the air at the level of ppm); and, more recently, ruggedized and compact versions of gas chromatographs coupled with mass spectrometers (GC/MS). Consequently, since activities involving these types of sensors have to be done prior to knowing the substance’s identity, these responders need to follow “worst-case” safety procedures such as donning a level A suit until information is available, via these sensors, for grading the status of the situation more commensurately with the hazards associated with the identified chemical(s). Furthermore, in light of the recent terrorist events involving chemical [1] and biological [2] agents both the complexity and the hazards associated with Haz/Mat activities have greatly increased. In response to these evolving hazards, our laboratory has undertaken the development a chemical sensor that combines Raman spectroscopy and the technique of lidar (light detection and ranging) to enable the short-range, non-contact detection and identification of solid ground contamination and liquid chemical spills [3,4,5].

Compared to other optical detection techniques such as fluorescence or infrared absorption, Raman detection has significant advantages for surface contamination assessment. Fluorescence profiles observed for molecules in either the liquid or solid phases tend to be broad (several nm or more in the UV) due to vibrational relaxation. Hence, the fluorescence signatures are not highly-distinctive, and identification based on fluorescence alone can be difficult. For infrared (IR) absorption, a strong IR absorber (such as water) on a surface can obscure significant portions of the absorption spectrum. Even the composition, texture, and shape of the surface can affect a measurement since the technique relies on light reflected from the surface. Hence, infrared absorption is better suited to sensing gases, with a highly reflective surface (such as a retro-reflector) placed at the end of the line-of-sight. Raman detection, on the other hand, relies on light scattered by the contaminants themselves. The signal generation does not depend on the

composition or shape of the surface. Furthermore, there is no strong absorption of water in the ultraviolet, so that solar-blind Raman detection is possible for compounds in aqueous solutions.

While Raman lidar has been the purview of the atmospheric sciences community for the interrogation of airborne chemicals, the study of fundamental aspects of atmospheric physics, and air pollution compliance, work in our laboratory has explored the new area of stand-off detection of liquid chemical spills and solid ground/surface contamination. Such “non-traditional” lidar application areas, where we define “non-traditional” as those uses not encompassing the atmospheric sciences (specifically detection and monitoring of airborne chemicals and aerosols), historically have been limited to the detection and mapping of oil slicks on open water surfaces [6,7,8,9] the high-resolution mapping of both terrestrial and ocean topography, and the monitoring of vegetation health [10,11]. Work conducted in our laboratory has extended the application area of “non-traditional” lidar by demonstrating the detection *and identification* of contaminants on various manmade and natural surfaces. Since this work represents a new venue for lidar involving both unique technical and scientific issues specific to the application of lidar to short ranges, we shall forgo a detailed discussion on these other non-traditional lidar applications, unless directly related to our present work, and instead direct the reader to the above cited papers and Review articles.

Work conducted in our laboratory has pioneered the application of lidar technology towards the *non-contact* (meters to ~ 500 meters), *in situ, real-time* (10s seconds to a few minutes) analysis of chemical contaminants (bulk and on surfaces) through Raman, pre-resonance Raman, and resonance-enhanced Raman spectroscopy. We believe that this novel application of lidar will open up new areas of environmentally-related research along with the development of innovative compliance monitoring technologies that offer an inherently safer chemical detection instrument(s) for First Responders as well as for chemical processing and environmental monitoring.

Since the primary platform for our research is Raman lidar, we will present a short introduction to lidar with a focus on Raman lidar followed by a corresponding introduction into Raman spectroscopy. However, since this review article is focused on the non-traditional application of Raman lidar, the reader is directed to the compendiums of Grant [12], Measures [13], Hinkley [14], and the SPIE Milestone Series [15] for a more thorough discussion of traditional Raman lidar and its very successful applications to the atmospheric sciences. Following the brief discussions of lidar and Raman spectroscopy, we will then discuss our work

on the detection and identification of liquids at “long” stand-off distances (defined as 0.5 kms or more) using a traditional Raman lidar platform, and at short distances (3 – 50 meters) using a specially designed mini-Raman lidar platform developed in our laboratory. We conclude with a discussion of the unique research areas (niches) that Raman lidar can open up and along with how these platforms could be used with other spectroscopic techniques (i.e., fluorescence and surface-enhanced resonance Raman Spectroscopy (SERRS)).

Background

Raman Lidar

Before we discuss the specific platform of Raman lidar, it is instructive to provide a brief background of the lidar principle and its generic configuration. At its most fundamental, lidar is simply the optical analog of pulsed radar. Just as in radar, there is a transmitter, a receiver and data processing subunit. In the specific case of lidar, the transmitter is typically a pulsed laser system operating in the IR (e.g., CO₂ laser), visible (dye lasers, OPO/OPA) or near-UV/UV (Nd:YAG, Nd:YAG-pumped dye lasers, Excimer lasers, OPO/OPA) spectral regions. Figure 1 shows a schematic of our Mobile Raman Lidar Van (MRLV) platform which, while specific to Raman lidar, contains the basic elements of lidar outlined above. The optical receiver telescope is typically either of a Cassegrainian or Newtonian design though other designs [13, 15] have been used. The collected return signal can then be sent to a variety of detection subsystems depending upon the desired information. For the detection of lidar signals, PMTs (photomultiplier tubes) with their inherently superior detection characteristics are the detector of choice whenever possible. In a simplified configuration (as would be used for acquisition of an aerosol concentration profile) the elastically backscattered signal would be directed to a single element PMT. In the event a more complex measurement is conducted (i.e., combined elastic and Raman lidar), the backscattered signals will be directed into a polychromators (i.e., a series of dichroic optics and single-element PMTs each dedicated to a specific wavelength/channel of interest) [16,17]. Again, depending upon the desired measurements, the high-speed, large dynamic range available with PMTs allow for operation in the current mode for strong signals or, in the case of very weak signals such as Raman scattering, in a photon counting mode. It is highly desirable to utilize electronics commensurate with the detector so as to maximize the spatial resolution and

signal intensity. Today, with the ubiquity of high-performance ADC systems and computers, return signals can be collected and either processed in near-real time or stored for further offline processing. This high-performance has allowed the realization of high-duty cycle lidar systems that are capable of providing 24/7 column monitoring [18,19]. This latter fact points to the level of maturity that lidar has achieved following its 3-decade development.

While, in principle, the experimental configuration is straightforward, there are many variations on this configuration scheme depending on the phenomena exploited and the measurement desired. For example, in contrast to the co-axial configuration depicted in Figure 1, some lidar platforms are bi-axial; that is, the transmitter and receiver are co-located, but sit side-by-side in the platform. Such configurations have the advantage that the amount field-of-view (FOV) overlap and the range at which the overlap occurs can be controlled. This is important because the $1/\text{range}^2$ signal dependence places severe dynamic range requirements on the detection system. Control of the overlap is generally referred to as optical or geometric compression [20]. For co-axial configurations, geometric compression is addressed by use of synchronized mechanical choppers or variable-range amplifier circuits. Depending on the phenomena being used, lidar platforms are capable of providing “range-resolved” or “path-integrated” measurements. The more useful of the two, range-resolved measurements monitor the laser pulse time-of-flight ($\text{range}/2 \cdot c$; the factor of 2 accounts for the return trip to the receiver) and the returning scattered laser light intensity. Since the return signal strength depends upon the concentration of a species along a particular line of sight, a spatial profile of the path taken by the laser pulse can be procured, where the spatial resolution achieved is limited by the detection system bandwidth and the laser pulse width. Most range-resolved lidar systems routinely achieve ~5-250 meter (200 MHz – 4 MHz) spatial resolutions. However, depending on the desired range, integration time, and phenomena exploited, the spatial resolution can vary outside these cited bounds. In contrast to “range-resolved” lidar, “path-integrated” lidar measurements provide a measure of signal attenuation a laser pulse undergoes from the transmitter, through the atmosphere, and back to the receiver (via aid of a retro-reflector or ground albedo). Despite the fact that “path-integrated” measurements necessarily lack spatial resolution, they possess superior detection sensitivity.

The phenomena that lidar platforms can exploit fall into two general categories, elastic scattering (for absorption measurements and aerosol density profiles), and inelastic scattering

(fluorescence and Raman spectroscopy). The phenomenon of choice in the atmospheric community is primarily absorption by specific target molecules due to the availability of large absorption cross-sections in readily accessible laser wavelengths. Leveraging these advantages translates to high-detection sensitivities on the order of low parts-per-million (ppm) [13,21,22,23] to low parts-per-billion (ppb) levels [24,25]. This type of absorption measurement is accomplished by using the differential absorption approach commonly referred to as DIAL (Differential Absorption Lidar) [26,27,28]. As the name suggests, the implementation of DIAL involves using two laser frequencies that are directed to the area of interest and their respective elastic return signals monitored: λ_1 located at a highly-absorbing wavelength for the chemical species-of-interest and λ_2 in a non-absorbing spectral region.

In contrast to the inherently large scattering cross-sections that characterize aerosols/particulates ($\sim 10^{-8} - 10^{-10} \text{ cm}^2$) which enable high spatial resolutions and long detection ranges to be achieved with aerosol lidar, Raman lidar systems while providing excellent spatial resolution suffer from severely limited range because of the very small Raman cross-sections ($\sim 10^{-29} \text{ cm}^2$). It is for this reason the traditional Raman lidar systems are typically limited to the detection and monitoring of percent-level species (e.g., N_2 , O_2 , water vapor), though there has been some success at detection of 100s ppm-levels of some atmospheric pollutants [29]. However, unlike aerosol lidar, Raman lidar offers the potential of discriminating chemical species through the exploitation of the unique vibrational spectral fingerprints that characterize molecular species.

The exploitation of Raman spectroscopy by lidar dates back to the mid 1960s when in 1967 Leonard [30] collected Raman returns from atmospheric nitrogen and oxygen using a pulsed nitrogen laser (337.1 nm). This was followed by a series of seminal works by Cooney [31], Melfi [32] and Inaba [33]. During the late 1960s and early 1970s these investigators improved upon the work of Leonard by increasing the detection range of N_2 and O_2 , and expanding the detection to include water vapor, pollutants such as SO_2 and the constituents of car exhausts. Since speciation was at the heart of these lidar platforms, special considerations had to be addressed that were not necessary with DIAL or aerosol lidar systems. Most notable of these considerations was the requirement to disperse the returning light into N_2 , O_2 and water vapor spectral regions. Since the fact that the Raman effect is a very weak phenomenon, care had to be given to maximizing the throughput while still retaining spectral discrimination and minimizing stray light. The most

successful Raman lidar platforms achieve a rejection ratio approaching 10^8 for N_2 and O_2 and 10^{10} for water vapor. These system characteristics are achieved through the use of dichroic mirror/narrow bandpass filter combinations utilizing PMTs in the photon-counting mode [13] and later with polychromators [17]. In addition to this, the small scattering cross-sections also required the employment of high-pulse energy laser systems. Back in the late 1960s and early 1970s this was limited to fundamental and doubled Q-switched Ruby lasers (694.4 and 347.2 nm, respectively). However, the advent of high-power, high-repetition rate Excimer lasers (351, 308, 248 nm), and Q-switched, frequency tripled and quadrupled Nd:YAG lasers (355 and 266 nm) have increased the number of chemicals detectable with Raman lidar [17, 34, 35, 36]. In addition, the development of laser systems operating at $\lambda < 300$ nm permitted interrogation in the solar-blind. In an attempt to evaluate the performance envelope of traditional Raman lidar, in the 1990s, Sedlacek *et al.* [37] and Ahmad [38] and co-workers revisited resonance-enhanced Raman scattering for detection range improvement. Despite the improvement in the scattering cross-section (which, for resonance-enhanced cross-section, can approach $10^3 - 10^5$ [*vide infra*]) only a marginal improvement was achieved in the detection range. However despite these technological advances, the utility of Raman lidar has been limited to the technical niche of water vapor profiling, extraction of aerosol properties if combined with elastic lidar and, if used in a Raman-DIAL platform [39,40,41,42], tropospheric ozone profiling.

To put the lidar technique on a theoretical footing, we have reproduced the well-known inelastic scattering lidar equation, which has been modified to reflect our focus on Raman lidar.¹³ [13]

$$P_i(R, \Delta R, \lambda_{exc}) = C \frac{\Delta R}{R^2} \frac{d\sigma^{Raman}(\lambda_{exc})}{d\Omega} n_i \exp\left\{ \sum_{j=1}^n \left[\sigma_j^{abs}(\lambda_{exc}) + \sigma_j^{abs}(\lambda_{Raman}) \right] \int_j(r) dr \right\} \quad (1)$$

The received power is $P_i(R, \Delta R, \lambda_{exc})$, which is a function of range R , spatial resolution ΔR , and laser excitation wavelength. The inelastic scattering is produced by molecule i with a Raman scattering differential cross-section of $\frac{d\sigma^{Raman}(\lambda_{exc})}{d\Omega}$ and a number density n_i over a range

increment ΔR . Both the transmitted laser light at wavelength λ_{exc} and the returning inelastically scattered light at λ_{Raman} are diminished due to absorption by molecules j with number densities n_j . The terms $\sigma_j^{abs}(\lambda_{Raman})$ and $\sigma_j^{abs}(\lambda_{exc})$ denote the absorption cross-sections of these

molecules at the Raman scattered wavelength λ_{Raman} and the excitation wavelength λ_{exc} . The constant C is an instrument constant (which includes information on receiver size, throughput efficiency, laser intensity, etc.). Although attenuation due to aerosols in the *return* path has been ignored, in a more thorough treatment this factor would have to be addressed [43,44]. The key points highlighted by Equation (1) that should be noted are (i) the $1/\text{range}^2$ dependence of the lidar signal strength, (ii) the proportionality of the signal strength on number density and molecular scattering cross-section and (iii) the exponential dependence of the transmitted laser light and back scattered signal on absorption and scattering losses while traversing the atmosphere. We will return to this equation in our discussion below on the application of Raman lidar to ground contamination detection and identification.

Raman Spectroscopy

When Raman lidar is applied to the detection and identification of substances at short-ranges (meters to 10s of meters), the first realization is that the Raman scattered return signal is sufficiently strong to allow acquisition of the entire Raman spectrum (spectral fingerprint) for chemical identification and quantification, while the small Raman cross-sections are an issue for long range detection. This advantage places unique demands on the detection subsystem (*Vida infra*), and requires that a usable spectral database of chemicals be available for automated chemical identification. However, despite the existence of commercially-available Raman spectral databases very few Raman spectra collected in the ultraviolet (UV) exist. Consequently, we have had to undertake the selected acquisition of UV Raman spectra of chemicals of interest in order to initiate the creation of a UV Raman spectral database for use by our Raman lidar unit.

Raman scattering is a two-photon process that was first observed by its namesake, C. V. Raman nearly 75 years ago [45]. In this inelastic process, an incident photon of energy $h\nu$ is destroyed upon collision with a molecule resulting in the simultaneous creation of an exiting (scattered) photon of energy $h(\nu \pm \nu')$, where ν' is the energy for the vibrational mode participating in the scattering process. It is in this way that Raman spectra reflect the molecular vibrational transitions and thus provide the same kind of molecule identification information as infrared (IR) spectra. If the final vibrational state lies above the initial state (i.e., $h(\nu - \nu') < h\nu$), then the observed Raman lines are referred to as Stokes, and anti-Stokes is they lie below, $h(\nu + \nu') > h\nu$. In addition, because the Raman phenomenon is an inelastic scattering process, the line positions of

the resulting Raman spectrum are independent of the excitation frequency, thereby providing flexibility in the choice of laser frequency, as in the case of using a laser wavelength shorter than 300 nm allowing signal acquisition in the solar blind region [46].

In general, normal Raman scattering cross-sections of gas phase molecules are on the order of 10^{-30} cm² Sr⁻¹ and possess a ω^4 -dependence on the excitation frequency [47]. Thus, going from a laser operating at 1064 nm to one operating at 266 nm results in an increase in the scattering cross-section of 256 times. In addition to this dependence, it is also possible to realize additional enhancement of the Raman scattering cross-section through the phenomenon known as pre-resonance and resonance-enhanced Raman scattering. These latter enhancements come about when there is significant coupling between a given ground vibrational state and an electronically excited state and can be as large as 10^6 , dramatically enhancing the vibrational modes of those parts of the molecular system that are directly coupled to the electronic transition. Pre-resonance and resonance-enhancement have been observed for many small molecules, larger aromatic molecules, aromatic amino acids, and nuclei acids by the research groups of Hudson [48], Spiro [49], Asher [50], Myers [51], and others [52,53,54,55,56]. Taken together, these studies have examined and subsequently established the underlying principles of resonance-enhanced Raman scattering. Since excellent review articles are available in the literature [47,57,58,59], readers interested in general aspects of resonance Raman spectroscopy are referred to these review articles. Here, we use chloride carbon compounds, such as CCl₄, C₂HCl₃ and C₂Cl₄ which are environmental important as examples to illustrate pre-resonance and resonance effects of Raman scattering.

CCl₄ is one of a number of volatile organic chemicals (VOCs) of interest that are hazardous to health. CCl₄ along with numerous other VOCs are tightly regulated and the development of in situ remote monitoring would be expected to aid in insuring regulatory compliance. Raman spectroscopy studies of VOCs like CCl₄ provide essential parameters for the Raman lidar platforms and also serve as an example to illustrate the pre-resonance enhancement phenomenon.

Absorption of CCl₄ between 15,000 and 40,000 cm⁻¹ is shown in Figure 2(A). As is shown in the figure, CCl₄ has a weak absorption near 40,000 cm⁻¹. The Raman cross-sections of CCl₄ below 30,000 cm⁻¹ have been reported in the literature [60], measurement of the cross-sections has been extended to 42,500 cm⁻¹ in our laboratory as shown in Fig 2(B) in order to have enough

spectral range for examining excitation profile by Albrecht A-term. In the specific case of pre-resonance of a strong allowed transition, the A-term enhancement should dominate. The pre-resonance excitation profile of the Raman cross-section for a totally symmetric vibration is described by the Albrecht A-term expression [61]:

$$I_{mn} = K \cdot \nu_0 \cdot (\nu_0 \pm \nu_{mn})^3 \cdot \frac{\nu_e^2 + \nu_0^2}{(\nu_e^2 \pm \nu_0^2)^2} \quad (2)$$

where K is a collection of frequency-independent factors, and ν_e is the frequency of the transition to the resonant excited state. A slight resonance enhancement, (*i.e.*, *pre-resonance*) is clearly evident. At 40,000 cm^{-1} excitation, the Raman cross-section of 459 cm^{-1} CCl_4 band (ν_1, a_1) is about a factor of two higher than one expected from ν^4 -relationship, while one of 314 cm^{-1} CCl_4 band (ν_4, f_2) is in agreement with expected ν^4 -dependent within experimental errors. Optical absorption spectra of CCl_4 show four broad bands peaked at 176, 140, 132.5 and 129 (doublet), and 112.4 nm. The 176 nm band is known as the “A” band having the valence shell assignment chlorine 3p \rightarrow 3p* (C-Cl). The other bands, 140, 132.5 and 129 nm are assigned as 4s, 4p and 4p’ Rydberg transitions, respectively [62]. A value of ν_e obtained from the A-term fit is 73.5 nm, which is higher than the ionization potential, 106.9 nm. It is important to point out that while the A-term fit using Eq. (2) results in a cross section frequency dependence that is in excellent agreement with the experimental data the approximations involved in Equation (2) can lead to overestimates of the transition energies of the lowest energy excited states important for the *pre-resonance* enhancement. The most important approximation to the present discussion is that the A-term fit assumes that one transition dominates the Raman intensities. In reality, a number of transitions can contribute to the polarizability tensor. These contributions could be of opposite sign and lead to partial cancellation of the contribution from pairs of transitions. The pre-resonant effect in ν_1 of CCl_4 may be due to contributions from many electronic excited states rather than form A band alone.

In addition to the environmental concerns regarding trichloroethylene (TCA) and tetrachloroethylene (TCE), these molecules provide illustrative examples of how dramatically the Raman scattering intensity of vibrational modes change due to resonant enhancement. As shown in Figure 3(A) and (B), Raman spectrum of C_2HCl_3 excited at 1064 nm has two prominent bands at 1589 cm^{-1} (C=C stretch) and 628 cm^{-1} (C-Cl stretch). The first absorption band of C_2HCl_3 has an extensive continuous region between 250 and 173 nm, with maximum intensity at about 195

nm, which can be assigned as $\pi(C=C) \rightarrow \pi^*(C=C)$ transition [62]. One would expect a strong enhancement of the C=C stretch to occur since the vibrational mode is more likely to couple with the $\pi(C=C) \rightarrow \pi^*(C=C)$ transition. UV Raman spectrum of C_2HCl_3 excited at 228.9 nm demonstrates this strong resonance effect on the 1589 cm^{-1} mode as shown in Fig 3(B). The 628 cm^{-1} mode was not observable in our experiments comparing with the ν_1 mode, which may be buried in the interference of quartz modes from the cell. *The Raman cross-section of 1589 cm^{-1} mode of C_2HCl_3 in liquid phase at 228.9 nm excitation was measured to be $1.61 \times 10^{-25}\text{ cm}^2\text{ molecule}^{-1}\text{ Sr}^{-1}$.*

For chloroethylene molecules, C-Cl bonding seems to shift $\pi(C=C) \rightarrow \pi^*(C=C)$ transition to low-frequency side. Excitation at 228.9 nm is expected to be closer to the resonance of $\pi \rightarrow \pi^*(C=C)$ transition for C_2Cl_4 than C_2HCl_3 . In other words, one can expect a stronger resonance effect on the C=C stretch mode for C_2Cl_4 than C_2HCl_3 at 228.9 nm excitation. There are five Raman active modes of C_2Cl_4 , 1571 cm^{-1} (ν_1, A_{1g}), 447 cm^{-1} (ν_2, A_{1g}), 237 cm^{-1} (ν_3, A_{1g}), 347 cm^{-1} , (ν_6, B_{1g}), and 512 cm^{-1} (ν_8, B_{2g}). It is similar to C_2HCl_3 in that only 1571 cm^{-1} mode was a prominent peak in 228.9 nm excitation, and *the Raman cross-section of ν_1 C_2Cl_4 mode in liquid phase is $6.41 \times 10^{-25}\text{ cm}^2\text{ molecule}^{-1}\text{ Sr}^{-1}$.* The Raman scattering of C=C stretch at 228.9 is about four time stronger for C_2Cl_4 than C_2HCl_3 , while the difference of absorption coefficient between C_2Cl_4 and C_2HCl_3 is less than a factor of two.

Raman Lidar Detection of Chemical Spills and Ground Contamination

Mini-Raman Lidar System (MRLS)

The primary objective behind the development of the Mini-Raman Lidar System (MRLS) was to enable the rapid, sensitive non-contact detection of surface/ground chemical contamination at *short ranges* (meters to <50 meters). The operational standoff distance for this system is quite short when compared to traditional lidar platforms whose operational range extends to many kilometers. However, for first responders in an urban environment, the reduced range is not a serious limitation since lines-of-sight are rarely more than a hundred meters. The development of this new instrument was possible due to the recent advances in compact, powerful lasers and optical array detectors as well as the availability of portable, yet powerful, computers for online data processing. The MRLS was designed to be portable and rugged enough for transport in a

standard mini-van and be deployable within minutes of arriving at a scene. The use of an ultraviolet (UV) solar-blind laser wavelength ($\lambda < 300$ nm), rather than a visible or near-infrared wavelength as used by Angel *et al.*[63] allows the MRLS to be used in daylight without interference from ambient light.

The work of Angel *et al.* [63] first demonstrated the efficacy of standoff Raman spectroscopy for detection and identification of bulk samples at short-ranges. In this study, two different lasers, an Ar⁺ laser (488 nm) and a diode-laser (809 nm), were used to generate the Raman scattering in the target substances, and a 40-mm diameter lens-based telescope collected the Raman signal. For 488 nm laser excitation, they obtained a signal-to-noise ratio of 250:1 for solid sodium ferrocyanide (Na₄[Fe(II)CN₆]) at a stand-off distance of 16.7 m after one minute of signal integration. Although these laboratory-based experiments demonstrated the potential of standoff Raman detection, the scope of the work conducted on our laboratory moved beyond that of Angel and coworkers. Specifically, we have designed and fabricated a Raman lidar platform with features that allow it to be used as a field instrument and that address the unique issues confronted when applying the lidar technique to short ranges (target distances comparable to focal length of the receiver system).

Design of the MRLS:

The “proof-of-principle” MRLS platform consists of a 65-lb. tripod-mounted optical head measuring 10” x 18” x 42” that is connected, via an umbilical cord, to a 24” x 24” x 30” power supply cart. The entire system, including an on-board water chiller, consumes about 800 W of line power. Both the size and the power consumption are suitable for deployment in the field inside a small van or mounted on a military vehicle. Figure 4 is a schematic of the optical head, which contains both the transmitter and receiver housed within a weather-resistant case. Comparison with the optical layout typical of traditional lidar units, Figure 4, allows the similarities and differences to be quickly discerned. The transmitted laser light and the Raman return signal pass through an anti-reflection coated UV quartz viewport on the front of the case. The entire optical system is mounted rigidly to a single platform to preserve the alignment of all of the components. Tilting the head varies the pointing direction of the MRLS. Figure 5 contains a picture of the MRLS.

The laser transmitter is a small, flashlamp-pumped 266 nm Nd:YAG laser (20 Hz, 7 mJ/pulse, 6 ns pulsewidth; New Wave Research). The beam waist is 3 mm at the exit aperture, with a divergence of 1 mrad x 2 mrad. At a distance of 3 meters, the laser spot is 6 mm x 9 mm. The spot size and pulse energy are sufficiently low to prevent dielectric breakdown or rapid heating of the target chemical, even if the chemical strongly absorbs the laser light. The average intensity of the laser is 200 mW/cm², which will not cause ignition of flammable substances. In addition to the UV laser, the MRLS has a 635 nm diode laser range finder that determines the distance to the target with an accuracy ± 2 mm.

The receiver is a 6-inch diameter, f/4 Newtonian telescope that is coaxial with the transmitted laser beam. The coaxial design ensures that the surface illuminated by the UV laser beam remains within the field-of-view of the telescope. Unlike traditional lidar platforms, the target ranges are comparable to the focal length of the receiver telescope. Consequently, these short-ranges require that the telescope primary mirror automatically adjust its position to keep the image plane at the entrance slit of the analyzing spectrometer. The primary is mounted on a rail glide and moved by a lead screw with a DC servomotor. The motor is interfaced to the laser range finder. The secondary is a 45-degree dielectric 266 nm mirror that passes nearly all of the visible light while reflecting the UV light into the spectrometer. The shortest standoff distance is three meters and is due to the limit of the travel range of the primary. The shadowing due to the secondary reduces the light collection by 15% for targets at 3 meters and by 10% for targets at 50 meters.

To prevent the strong, elastically-scattered laser light from obscuring the weaker Raman signals, a sharp-cut edge filter (Barr Associates) is placed between the receiver telescope and the spectrometer to reject the 266 nm light collected by the telescope. The transmission-to-rejection ratio is 10⁵:1, with the 50% transmission point located 350 cm⁻¹ to the red of the 266 nm line. The transmission at the Raman-shifted wavelengths is about 80%.

The analyzing spectrometer is a 0.25 m, f/4 system designed to be compact and lightweight yet have sufficient resolution and stray light rejection to collect Raman spectra. The grating is a 2380 groove/mm concave holographic grating (American Holographic). This type of spectrometer uses a single curved optic to reduce the complexity of the alignment. The spectrometer has no moving parts, so that the spectral window is fixed. Small adjustments in the angle of the grating can shift the position of the spectral window. Finally, a gated, intensified CCD (Andor InstaSpec

V) captures the Raman spectrum from 650 cm^{-1} to 3650 cm^{-1} to the red of the laser line (i.e., Raman Stokes lines). The CCD array is 1024×256 pixels, with the Raman spectrum dispersed along the longer (horizontal) dimension. The signal in the 256 vertical pixels is binned to produce a single channel signal. A plot of binned signal versus channel number forms the Raman spectrum. The channel numbers are then calibrated to the Raman shift in cm^{-1} . The spectral resolution of the MRLS is 22 cm^{-1} full-width half-maximum (FWHM), as determined by the 253.6 nm line of a mercury pen lamp. While this is sufficient for identifying the spectral fingerprints of a number of chemicals, higher resolution is preferable for distinguishing chemicals with similar Raman spectra or resolving the components of a complex mixture of chemicals.

Data acquisition and analysis are controlled by a laptop computer (Gateway Solo with LabVIEW software). A library of Raman spectra of pure samples taken with the MRLS is stored for use in substance identification. A simple form of a constrained least squares fit with a library of chemicals has already been tested successfully on the MRLS. The program is able to identify binary mixtures of the chemicals in real time. In principle, a mixture of many chemicals can be identified and quantified. The fundamental limitations are the spectral resolution of the spectrometer and the dynamic range of the array detector (40 dB). Work is currently underway to adapt a more sophisticated pattern recognition algorithm to the MRLS control program for reliable, automated, real-time identification.

Performance of the MRLS:

The spectral resolution of the MRLS is 22 cm^{-1} full-width half-maximum (FWHM). Figure 6 shows that the current MRLS is capable to detect and identify trimethyl phosphite (TMP), dimethyl methylphosphonate (DMMP), and diisopropyl methylphosphonate (DIMP). Raman spectra of these neat phosphate compounds are recorded at a stand-off distance of 2 meters from MRLS. The pathlength of the samples is 10 mm, and the signal integration time is 60 s for a 20 Hz Nd:YAG laser (266 nm , 100 mW average power). There is a very weak absorption of these phosphite compounds at 266 nm ($< 0.4\text{ M}^{-1}\text{ cm}^{-1}$) and the Raman cross-sections are in the order of $10^{-28}\text{ cm}^2\text{ molecule}^{-1}\text{ Sr}^{-1}$ for the CH stretch modes. It is clear that the current MRLS is sufficient for identifying the spectral fingerprints of a number of chemicals, but higher resolution is preferable for distinguishing chemicals with similar Raman spectra or resolving the components of a complex mixture of chemicals. The resolution depends on a combination of the entrance slit

width, the dispersion of the spectrometer, the pixel size of the array detector, the spatial resolution of the intensifier, and the quality of the image produced by the concave grating. Presently, the limiting factor appears to be the resolution of the image produced by the grating, as all of the other factors indicate that a FWHM of approximately 10 cm^{-1} is possible. We are currently investigating ways to improve the image quality.

As an initial test of the sensitivity of the MRLS at shorter ranges, we placed a film of acetonitrile onto the Teflon sheet and probed it at a standoff distance of three meters for five seconds. The spectrum is shown in Figure 7, with the modes of Teflon and those of the acetonitrile labeled accordingly. Teflon has a well-defined, strong Raman spectrum with several features: a sharp line feature at 729 cm^{-1} (marked $\square_k(\text{CF}_2)$ and assigned to symmetric F-C-F stretching mode (A_1)), three features between 1215 and 1379 cm^{-1} related to an antisymmetric F-C-F stretching mode (E_1 , $\square_b(\text{CF}_2)$, 1215 cm^{-1} peak), C-C stretching modes (E_2 , $\square(\text{C-C})$ 1295 and A_1 , $\square_b(\text{C-C})$ 1379 cm^{-1}), two features attributed to a F-C-F twisting mode (A_1 , $\square(\text{CF}_2)$) at 291 cm^{-1} and an unresolved pair of F-C-F bending modes ($A_1 \oplus E_2$, $\square(\text{CF}_2)$) near 383 cm^{-1} . The 576 cm^{-1} mode is assumed due to a defect structure of Teflon [64]. Prominent Raman bands of acetonitrile are 918 cm^{-1} ($\square_4(\text{C-CN})$ stretch), 1342 cm^{-1} ($\square_3(\text{CH}_3)$ deformation), 2253 cm^{-1} ($\square_2(\text{C}\equiv\text{N})$ stretch) and 2942 cm^{-1} ($\square_1(\text{C-H})$ sym. stretch), and all of these prominent bands have a_1 symmetry. The Teflon spectrum shows that surfaces that are interrogated for contamination may themselves produce a Raman fingerprint. As can be seen, the thin film of acetonitrile is clearly discernible from the Teflon Raman signature. This demonstrates the inherent strength of vibrational spectroscopies: Speciation. The Raman cross section of C-CN stretch (918 cm^{-1}) is $1.92 \times 10^{-29}\text{ cm}^2\text{ molecule}^{-1}\text{ Sr}^{-1}$ for liquid phase acetonitrile. The thickness of the acetonitrile film is calculated by comparing the size of its Raman fingerprint to that of a known quantity of acetonitrile at the same standoff distance. The average film thickness of the acetonitrile is estimated to be $90\text{ }\mu\text{m}$. This result demonstrates for the first time the stand-off detection of a thin chemical film. It is necessary to point out that there is no resonance enhancement for acetonitrile excited at 266 nm . One could expect a great increase in detection sensitivity when the advantage of UVRR is fully exploited.

While there are significant advantages for employing an ultraviolet excitation source for the acquisition of Raman signatures, there are potential problems with laser-induced fluorescence of the contaminants and/or the surfaces which would complicate both the signal acquisition and the data reduction since fluorescence can be much stronger than Raman scattering thus obscuring

the Raman fingerprints of chemicals. Of special concern for the present Raman lidar application is the issue of bio-fluorescence, since the MRLS is to interrogate surface contamination *in situ*. The fluorescent bands of plant chlorophyll lie significantly far to the red of the 270-nm-to-300-nm region, where the Raman spectra are located. The nearest band is centered at 440 nm [65]. Hence, they will not interfere with the Raman detection. However, certain amino acids do fluoresce in the UV. Tryptophan, an amino acid found in many forms of bacteria, is one such important case. The tryptophan fluorescence maximum is near 350 nm, with a broad profile extending into the Raman spectral window.

In the case of tryptophan fluorescence, a change of laser excitation wavelength from 266 nm to less than 253 nm can move the Raman spectrum into a nearly fluorescence-free region [66]. The reason is that the Raman-shifted wavelengths track the change in laser wavelength while the fluorescence profile of the tryptophan remains fixed, regardless of the change in the UV laser wavelength, due to the fast non-radiative decay of the excited electronic states. Hence, the Raman spectrum is “blue-shifted” away from the tail of the tryptophan fluorescence.

This blue-shifting technique is illustrated in Figure 8 for the chemical cyclohexane placed onto a sample of topsoil. The spectrum in Figure 8(a) is that of pure cyclohexane excited by the pulsed 266 nm laser in the MRLS. Figure 8(b) is the spectrum of cyclohexane on soil, also obtained with the 266 nm laser. The soil is rich in humus and other biological materials. As is clearly observable, the tryptophan fluorescence background makes it difficult to identify the peaks of the Raman fingerprint. In Figure 8(c), the Raman spectrum of the same sample collected by the MRLS, with a table-top frequency-doubled Ar⁺ laser at 248 nm replacing the 266 nm Nd:YAG, is shown. The reduction of the bio-fluorescence from the soil to a negligible level allows the Raman spectrum of cyclohexane to be clearly discerned.

Although they were performed in a controlled environment, these experiments have helped to define the operational envelope of the MRLS and to identify further development criteria. The Mini-Raman Lidar System is capable of detecting and automatically identifying films several microns thick at stand-off distances of meters and bulk liquids (such as small puddles) at distances of tens of meters with signal acquisition times less than one minute, regardless of ambient visible light.

In estimating the ultimate sensitivity of the MRLS, we assume that the signal-to-noise ratio is limited primarily by the signal shot noise. Hence, it is necessary to verify the operating

parameters for which this assumption is valid. One parameter is the size of the signal compared to the inherent detector noise. Variations in detector response and variations in the dark current from one pixel to another (or “fixed pattern noise”) are two forms of detector noise. However, these can be removed by normalizing the signal with respect to the measured pixel response and by subtracting the dark current background from the signal. The real sources of detector noise are the “read out” noise (i.e. noise associated with analog to digital conversion of the signal) and the shot noise associated with the dark current. The read out noise is typically 1 count, while the dark noise is approximately $3.5 \text{ counts} \cdot (\text{Hz})^{1/2}$ when the CCD chip is cooled to -40 C. For one second of signal integration, the RMS noise is approximately 3.7 counts. For signals of this size, the detector noise becomes significant.

Another parameter is the signal integration time or, for a pulsed laser, the number of laser shots. For a shot-noise limited system, the signal-to-noise ratio (SNR) scales with the square root of the integrated signal and is proportional to the square root of the number of laser shots (N), (e.g., $SNR \propto \sqrt{N}$). For a log-log plot of SNR vs. N, the relation is simply a straight line with a slope of $1/2$. However, if there are other sources of noise (such as laser speckle) that limit the growth of the signal-to-noise ratio as a function of time, this relationship breaks down.

Figure 9 shows the SNR for the 732 cm^{-1} mode of Teflon as a function of laser shots from one shot up to 4,000 shots. For the 20 Hz Nd:YAG laser in the MRLS, this corresponds to a variation in signal integration time from 50 ms to 200 seconds. The SNR is defined as the baseline-corrected area under the 732 cm^{-1} mode divided by the RMS noise of the baseline. Over the first two decades of integration time, the measured SNR follows the characteristic behavior of a system limited by signal shot noise. However, at longer integration times, there appears to be some deviation from the shot noise limit. As this long integration data is preliminary, it will be reexamined to confirm the validity of this deviation. Nonetheless, for the integration times expected for the MRLS in the field (< 1 min or < 1000 laser shots), the estimates of sensitivity (both theoretical and empirical) for which shot noise is the dominant noise source appears to still be valid.

For short-range detection of surface or ground contamination, the angle of the laser beam with respect to the normal of the surface is likely to be large (fifty degrees or more). Most of the samples interrogated with the MRLS were illuminated at near normal incidence. To observe the effect of the interrogation angle on the Raman return signals, we have measured the Raman

spectrum of a sheet of Teflon. The angle between the laser beam and the normal of the surface was varied from 0° to 75°. The size of the Teflon sheet was large enough to ensure that the laser beam does not overfill it, even at the large angle of incidence. The area under the 732 cm⁻¹ peak after one minute of signal interrogation is shown as a function of angle in Figure 10. As is clearly seen, the Raman signal drops by nearly a factor of seven between incidence at 0° and at 75°. To explain this effect, we have calculated the loss of collected Raman light due to “defocusing”. As the interrogation angle increases, the laser beam spans more of the length of the Teflon sheet. When the receiver telescope forms an image of the illuminated area on the Teflon, the edges of the laser beam are out of focus with respect to the center of the laser beam. For the standoff distance of 2.25 m, this effect can be significant. The depth of focus of the telescope is shorter than it would be for a longer-range lidar receiver. Hence, less of the Raman scattered light is able to pass through the spectrometer slit, and the signal decreases. The solid line in Figure 10 shows a model calculation of the Raman signal strength as a function of interrogation angle (i.e., variations in the slit transmission caused by this defocusing effect). However, as is clearly discernible in this figure, the slit transmission model alone cannot completely explain the angular dependence. It is interesting to note that the remaining differences between the slit model and the experimental data can be reconciled when a Lambertian cosine dependence is combined with the slit transmission model [66].

The sensitivity limit of the MRLS for acetonitrile can now be estimated from an appropriately modified version of the lidar equation and compared to the sensitivity extrapolated from the fingerprint of the neat sample in the 10 mm cell. The lidar equation is:

$$S = G \cdot n \cdot l \cdot \frac{d\sigma_R}{d\Omega} \cdot I \cdot \tau_{filter} \cdot \tau_{slit} \cdot \tau_{spec} \cdot \tau_{tel} \cdot \tau_{qe} \cdot \frac{A}{r^2} e^{-\alpha_{laser} r} \cdot e^{-\alpha_{Raman} r},$$

where S is the detected signal (counts/s), G is the gain of the intensifier (50counts/photoelectron), n is the molecular number density of acetonitrile ($8 \times 10^{21} \text{ cm}^{-3}$), l is the thickness of the chemical on the surface, $\frac{d\sigma_R}{d\Omega}$ is the differential Raman cross-section, I is the rate of arrival of photons at the target, τ_{filter} is the transmission of the UV edge filter (approximately 80%), τ_{slit} is the spectrometer slit transmission (about 3%), τ_{tel} is the transmission efficiency of the receiver telescope (75%), τ_{spec} is the throughput efficiency of the spectrometer (approximately 20%), τ_{qe} is the quantum efficiency of the detector (25%), A is the area of the receiver telescope primary,

α_{laser} is the absorption coefficient of air at the laser frequency, α_{Raman} is the absorption coefficient of air at the Raman return frequency, and r is the distance from the receiver telescope primary mirror to the target.

For positive identification of a chemical, a SNR of 10:1 for most of the Raman modes is desirable and will be considered the lowest acceptable limit. The sensitivity limit is estimated for the 918 cm^{-1} mode, which has a cross-section of $2 \times 10^{-29}\text{ cm}^2/\text{molecule}\cdot\text{ster}$ for 266 nm excitation (100 mW average power). The other modes of acetonitrile have larger cross-sections and should have signal-to-noise ratios at least as large. The RMS detector noise is 3.7 counts for 1 second of signal integration, and it is folded into the calculation of the total noise. For a stand-off distance $r = 3\text{ m}$, the attenuation of both the laser beam and the Raman return light by atmospheric ozone is negligible. The result is that the MRLS could detect an acetonitrile film approximately 1 μm thick at a stand-off distance of 3 m after 1 second of signal integration. The molecular weight of acetonitrile (CH_3CN) is 51. For a 1 μm film of acetonitrile, the surface coverage is $0.6\text{ g}/\text{m}^2$. Extrapolation of the 918 cm^{-1} mode in the acetonitrile spectrum of Figure 7 yields a minimum detectable film thickness of 2 μm , or a mass coverage of $1.5\text{ g}/\text{m}^2$, in good agreement with the theoretical limit. As the signal-to-noise curve in Figure 9 suggests, these limits could be extended further in direct proportion to the signal integration time. In addition, with careful attention to the size and shape of the UV laser beam, it may be possible to improve the transmission of the Raman signal through the slit and increase the sensitivity further [67].

The data collected with the MRLS suggest that given careful consideration to issues such as platform volume and weight, power requirements, and further optimization of the optical train, a fieldable version of this short-range chemical sensor could be used by a non-expert, “End-User” [5,67].

Mobile Raman Lidar Van (MRLV)

While conducting work on the MRLS the question regarding longer range (>100 meters) detection and identification of bulk chemical spills (as might be required in the event of a chemical leak from a railroad tanker, or the rupture of a pipeline) was addressed. Since the MRLS was specifically designed for very short ranges, a series of experiments were carried out using the BNL Mobile Raman Lidar Van (MRLV). Just as in the case of the MRLS, the MRLV combines the molecular fingerprinting technique of Raman spectroscopy with the stand-off capability of conventional lidar systems to enable first responders to identify the contaminants involved in a

spill while still maintaining a stand-off distance of 0.5 km or more. The fundamental difference between the two active remote sensing platforms is that the MRLV was originally designed as a traditional Raman lidar system (*Vide supra*). However, acquisition of a Raman signature from liquid chemical spills required no reconfiguration of our existing Raman lidar platform.

The application of lidar to the long-range (100s of meters) detection of chemical spills has been successfully applied to the detection of oil spills/slicks on open water. In the 1980s, Hoge and Swift [6,7,8,9] and Measures [13] reported on the fluorescence-based detection of oil slicks and film thickness using the Raman return signal from water and fluorescence from the oil. Specifically, these researchers used the attenuation of the water Raman backscatter as a measure of the oil thickness above the water. Later, Hengstermann and Reuter [7] used fluorescence lidar from oil on the sea surface to estimate oil thickness. While this later approach leveraged the inherently large fluorescence cross-section, this approach did suffer from limitations associated with fluorescence emitted by dissolved organic matter (DOM). More recently, Yamagishi et al., have continued exploring fluorescence lidar by developing and testing of a compact lidar unit for oil spill detection on open water [8].

MRLV Design:

The Brookhaven MRLV system is shown schematically in Figure 1 as a typical example of a Raman lidar platform. The entire system (transmitter, receiver, electronics, cooling systems, and diesel-electric generator) is contained within the modified RV and its tow trailer and is self-contained. The MRLV is completely mobile and tows a 40 KW diesel generator that supplies all of the MRLV power requirements.

The laser source can be either a frequency-quadrupled Nd:YAG laser (Spectra Physics GCR-170, 266 nm, 30 Hz rep rate, 3-4 ns pulse width) or a Nd:YAG pumped dye laser (Quanta Ray, PDL-1) should wavelength tunability be required. The beam diameter is approximately 8 mm with a divergence of 1 mrad before it enters a 1:3.5 beam expander (BX in Figure 1). The expander increases the beam size in the near-field but reduces the divergence to 0.3 mrad. The beam diameter is approximately 150 mm at a range of 533 m. The receiver is a 40 cm (16”) diameter Cassegrain (f/15). The ratio of the target range to focal length of the telescope determines the “demagnification” of the far-field laser spot onto the entrance slits of the spectrometer. For a range of 533 m, the “demagnification” factor is ~750. Hence, the 150-mm-

diameter far-field laser spot forms an image 200 microns in diameter on the spectrometer slits. The transmission through the 100-micron-wide slit is ~60%.

The transmitter and receiver are coaxial so that no mechanical adjustments are required to keep the laser spot within the field of view of the telescope. Both the transmitter and receiver are fixed to a single optical table. A flat 40 cm x 60 cm aluminum-coated front surface mirror both directs the expanded laser beam to the target and reflects the return light into the telescope. The angular resolution of this turning flat is 0.007 degree, which corresponds to 6.5 cm at a range of 533 m. An aluminum-coated pick-off mirror placed on a precision flip mount directly before the spectrometer slit directs the light from the telescope into a color CCD camera, thereby allowing the operator to align the turning flat by viewing the video image of the target. The mirror flips out of the optical path when the Raman spectra are acquired.

Unlike some other Raman lidar systems [16,17,18,41,40] which utilize a polychromator configuration (i.e., bandpass filters and photomultiplier tubes), the MRLV employs a single-grating spectrometer and an array detector to capture the entire Raman spectrum. Although the array detector is not as sensitive as a photomultiplier tube, the ability of the array detector to capture all Raman peaks simultaneously permits rapid identification of a wide range of chemicals. The spectrometer is a single stage 0.46 meter monochromator (JY-Spex HR-460) with 2400 g/mm grating blazed at 250 nm. The dispersion is 0.45 nm/mm. As with the MRLS, the MRLV employs deep, UV-edge filters centered at 266 nm (Barr Associates) for attenuation of the elastic signal strength prior to entering the spectrometer. The detector is an intensified CCD with a 1024 x 256 rectangle pixel array (Andor, Insta Spec V). The light is dispersed along the longer horizontal dimension, and the signal is summed over the 256 vertical pixels to form a 1024-channel Raman spectrum. The resolution of CCD detector is 2.8 cm⁻¹ per pixel, while the spectral resolution of the UV spectrometer is about 11 cm⁻¹ with 100 μm entrance slit.

The intensifier acts as a fast shutter (minimum gatewidth of 20 ns) that operates in sync with the pulsed Nd:YAG laser. Range-resolved measurements are performed by varying the time delay between the laser light pulse exiting the MRLV and the trigger pulse for the intensifier. Data acquisition and analysis are controlled by LabVIEW running on a Windows-based desktop PC. A library of Raman spectra of pure samples taken with the MRLV is stored for use in substance identification.

MRLV Performance:

The initial tests of the MRLV were chosen to demonstrate its ability to detect and identify solids and liquids at distances on the order of 0.5 kms. As an example of the detection of solids, a Teflon target is placed at 533 meters and interrogated with the 266 nm laser. The spectrum in Figure 11(A) is that of the Teflon target placed at a range of 533 meters. The HR-460 spectrometer is set so that the central wavelength of the spectral window is 276 nm. The spectrum shown in Figure 11(A) is the total signal acquired in 150 seconds. The peak intensity of 1379 cm^{-1} is about 260 counts/second under current experiment conditions.

The signal-to-noise (S/N) ratio for the spectrum is 50:1 for the peaks near 1000 cm^{-1} , which is in accord with the results expected for a shot-noise-limited system. Since the collection efficiency of the receiver decreases as the square of the range, it should be possible to collect Raman data with a S/N ratio of 5:1 at a distance of over a kilometer, excluding other range-limiting effects, such as ozone absorption or light scattering by dust and aerosols. Hence, it is possible to obtain clear Raman signatures of a solid target that is a strong Raman scatter, such as Teflon, at kilometer ranges.

Figures 11 (B) and (C) show Raman returns from two neat liquid samples, also at a range of 533 m. The samples are cyclohexane and acetonitrile, respectively. These common solvents are placed into a liquid cell with 6 mm-thick, UV-grade quartz windows and a 19 mm pathlength. The clear aperture of the cell is 23 cm to accommodate the size of the laser beam at the target. However, only a portion of the Raman light from this aperture is detected due to the finite width of the spectrometer entrance slit. (The height of the slit is sufficient to pass all of the light scattered by the target.) The illuminated area that is detected by the MRLV is approximately 70 cm^2 . The absorption of these samples is negligible for wavelengths below 260 nm, so that the full thickness of the liquid sample is interrogated. The sampled volume is 140 cm^3 .

An empirical estimate of the detection limit of the present version of the MRLV is now possible. All of the detection limits are expressed in mass coverage per unit area (g/m^2). The densities of cyclohexane and acetonitrile are $0.78\text{ gm}/\text{cm}^3$, typical of most industrial solvents. The sampled mass is 115 grams. The cyclohexane [68] and acetonitrile [69] C-H stretching features due to symmetrical and asymmetrical C-H stretching modes and which peak near $\sim 2900\text{ cm}^{-1}$ are quite strong. Raman peaks due to C-C vibrational modes and CH_2 rocking, twisting, and scissoring modes lie between 802 and 1446 cm^{-1} . These features are from ten to twenty times less

intense than the C-H stretch features near 2900 cm^{-1} . For cyclohexane, the S/N ratio of these C-H peaks exceeds 100:1, while for the smaller peaks the S/N ratios are about 35:1. For this estimate, a minimum detection S/N limit of 5:1 is required for the weaker peaks so that the *entire* Raman fingerprint is discernible. (The C-H stretch peaks in most organic molecules have similar Raman shifts so that other Raman peaks are necessary for specific identification.) For this detection limit, the integration time could be reduced from 150 seconds to 60 seconds and the sampled volume could be reduced by a factor of 20, since the S/N ratio varies as the square root of the signal for a shot-noise limited system. This corresponds to a sampled mass of 6 g spread over 70 cm^2 . Hence, the minimum detectable mass coverage at a range of 533 m is 850 g/m^2 for one minute of signal integration. Small puddles of a liquid leaking from a storage tank or a railroad car could be identified at a standoff distance of half of a kilometer or more.

The Figures 12 (A) and (B) show low frequency vibrational Raman features for cyclohexane with carbon disulfide (1% by volume in cyclohexane) and acetonitrile with carbon tetrachloride (10% by volume in acetonitrile) respectively. These spectra show the power of the MRLV to detect mixtures at long ranges and provide spectral discrimination. This capability is important for identification of spills involving unknown mixed wastes. They also illustrate the effect of resonance enhancement⁵⁶ in the case of CS_2 , which increases the sensitivity of the system for a few materials like CS_2 . Although the relative quantity of CS_2 is small, its Raman mode at 652 cm^{-1} is comparable in magnitude to the cyclohexane features. The volume of CS_2 sampled by the MRLV for 150 seconds is 1.5 ml, which corresponds to a mass coverage of 246 g/m^2 . Using the criteria of S/N ratio equal to 5:1 after sixty seconds of integration, the sensitivity limit is approximately 70 g/m^2 , more than a factor of ten better than that of cyclohexane. CCl_4 does not undergo significant resonant enhancement. However, CCl_4 features (marked in Figure 12 (B)) are detected along with atmospheric nitrogen and oxygen features.

These estimates of sensitivity are empirical. Theoretical estimates based on the lidar equation suggest an ultimate sensitivity of several g/m^2 at 0.5 km after sixty seconds of signal integration. The discrepancy is most likely due to scattering losses of the transmitted laser beam and the return signal due to aerosols. Due to logistical considerations at the lidar test range, all of the tests of solid and liquid samples were conducted between 8 P.M. and 12 A.M in early May. While the weather was typically clear on these evenings, the proximity to the ocean made the measurements vulnerable to light marine fog that is common during the spring and autumn.

Periodic measurements of N₂ and O₂ returns during the experiments confirmed a decrease in the Raman signal by nearly two orders of magnitude over that measured during the afternoon hours. The Raman signals for liquids and solids, and the empirical sensitivity estimates, represent non-ideal weather conditions. It should also be noted, that the Raman returns from atmospheric nitrogen and oxygen provide a means of correcting the measurements for this attenuation and obtaining quantitative estimates of the target substance.

Detection and identification of bulk quantities of unknown solids and liquids at ranges on the order of a kilometer are possible with a mobile, self-contained lidar van. The use of a solar-blind UV Raman fingerprinting technique allows identification and quantification with no prior information about the target substances and no interference from ambient sunlight. With a high-sensitivity, low-noise optical array detector, such as an image-intensified CCD, a modest amount of UV laser power can generate a clear Raman signature in sixty seconds or less. For liquids, empirical estimates of the minimum detectable mass coverage are approximately 800 g/m² at a range of 0.5 km after one minute of integration. Raman returns from atmospheric nitrogen and oxygen provide a real-time calibration of the MRLV sensitivity.

As shown in Figure 13, the MRLV can be used as a traditional lidar platform for detecting chemicals in atmosphere *without any modification*. We have also used the MRLV to perform Raman-Dial measurements which will be described somewhere else.

Future Applications

In an interesting twist on the experiments carried out in our laboratories, McCabe et al. [70] have reported the results of their initial exploration of utilizing SERRS for meters to 10 meters detection. Specifically this approach involves the marriage of resonance-enhanced Raman spectroscopy and surface-enhanced Raman spectroscopy. In contrast to resonance-enhanced Raman scattering (*infra supra*), surface-enhanced Raman spectroscopy arises from interactions between an analyte and a roughen metal surface. While many mechanisms have been proposed, two major types are generally agreed to be responsible for the enhancement: a) an electromagnetic effect associated with large local fields caused by electromagnetic resonances occurring near metal surface structures (surface plasmons), and b) a chemical effect involving a scattering process associated with chemical interactions between the molecule and the metal surface [71]. The SERS phenomenon is typically observed with roughen coinage metals (Ag, Au, and Cu) though Weaver

and co-workers have demonstrated SERS in ultra-thin layers (typically 10 monolayers) of non-coinage metals overlaying a SERS-active metal (coinage) [72]. As is self-evident by the name, surface-enhanced resonance Raman spectroscopy (SERRS) combines to two enhancement effects. This is typically accomplished by absorbing a dye molecule on a SERS-active surface. The major advantage of doing this is that it enables a variety of chromophores to be used.

Unlike the systems developed and tested in our laboratories, the McCabe et al. [70] work employed a bistatic configuration where a 532 nm doubled Nd:YAG laser (3.6 mW) was used to illuminate 4(5'-azobenzotriazolyl)-3,3-dimethoxyphenylamine (ABT DMOPA) particles dispersed in polyvinyl acetate and varnish. The probe head (receiver) was based on telephoto or CCTV lens that was fiber optically-coupled to a Renishaw 100 system. A photo of this handheld system along with Zemax-based raytrace calculations of this system are shown in Figures 14 and 15. As shown in Figure 16, following a 20-second integration time, a discernable SERRS spectrum from ABT DMOPA was acquired at stand-off distances out to 10 meters. It is easy to envision this work as a precursor to the generation of specially-prepared surfaces that could be used to preferentially collect (concentrate) vapors that could then be interrogated with a short-range Raman lidar-like system. Such a system would possess the advantages of providing an End User an in situ measurement, time-integration of the event(s), exploitation to two possible enhancement mechanisms for detection and the inherently safer sensing configuration of stand-off detection and identification.

In an effort to maximize the utility and field-harden a MRLS-like unit, Sedlacek and Higdon and co-workers [67] are developing an engineered variation known as LISA (Laser Interrogation of Surface Agents) as a short-range, field-deployable unit for “on-the-move” detection of low-vapor pressure chemical agent contamination on a battlefield. In contrast to the MRLS unit, the LISA system will utilize a KrF Excimer laser (for suppression of the tryptophan bio-fluorescence as discussed earlier), and a fiber optic coupling between the receiver telescope and the spectrometer thereby dramatically improving the coupling efficiency. In addition, LISA will possess a 205-mm Pressman-Carmichel based Cassegrainian receiver telescope and will be optimized for < 2 meter stand-off distances. Finally, an integral part of this fieldable system will be a spectral-database and associated spectral pattern matching algorithm for automated detection and identification of acquired Raman signals.

Finally, a very small, and thus short-range, MRLS-type instrument could be part of a payload that was sent to Mars in order to expand upon NASA's efforts to learn more about the Mars environment and surface materials by enabling remote sensing [73]. Even at detection stand-off distances of 2-4 meters, a mini-Raman lidar payload would provide a Mars surveyor instrument greater sensing range since the surveyor itself would not have to be brought into contact with the material of interest as has to be done now. Back on earth, this type of chemical sensor could be used as a forensic tool to aid law enforcement efforts towards drug interdiction and the illegal dumping of hazardous wastes and materials and, as pointed out above, a larger version of this sensor could be used in the event of a leak from a railroad tanker, or the rupture of a pipeline, or any other major incident involving the accident or deliberate release of hazardous chemicals.

Conclusions

We have both presented and discussed standoff chemical sensing instruments and associated experimental results that represent a paradigm shift for the *in situ* analysis of chemical compounds on surfaces. The existing platforms (MRLS and MRLV) used to perform these proof-of-principle experiments represent "Brass-broad" systems that were employed to perform these proof-of-principle experiments. While our work on this unique application of Raman lidar is now resulting in the fabrication of dedicated End User instrumentation and on the exploration of combining active short-range detection and identification with novel, prepared surfaces, this new research area is fertile with many questions that still require investigation.

Acknowledgements:

The works presented in the article are collective contributions and careful thoughts of many of our colleagues in the group, especially for Dr. Mark Ray's contributions in MRLS. We would also like to thank Drs. Carl L. Chen, H. K. Fung and M. Ruckman for their help while at BNL and Dr. G. Thomson for the preprint on their SERRS work and private communications of preliminary results. This work was performed under the auspices of the U. S. Department of Energy under Contract No. DE-AC02-98CH10886.

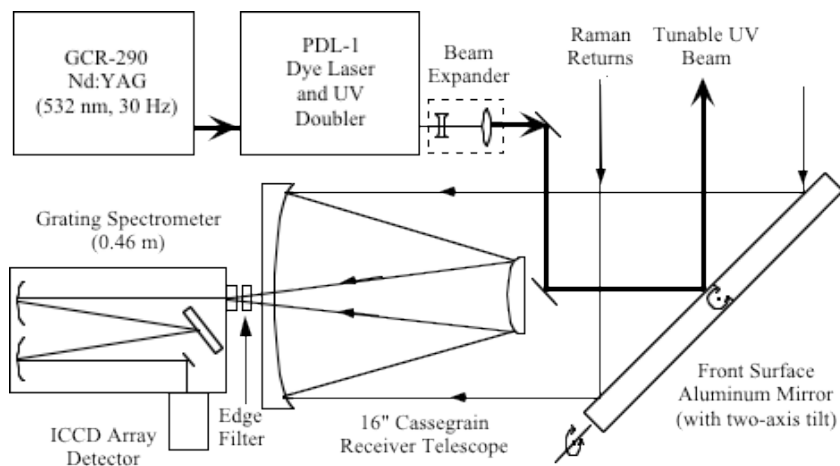


Figure 1: Schematic of Optical Configuration used in BNL's Mobile Raman Lidar Van (MRLV)

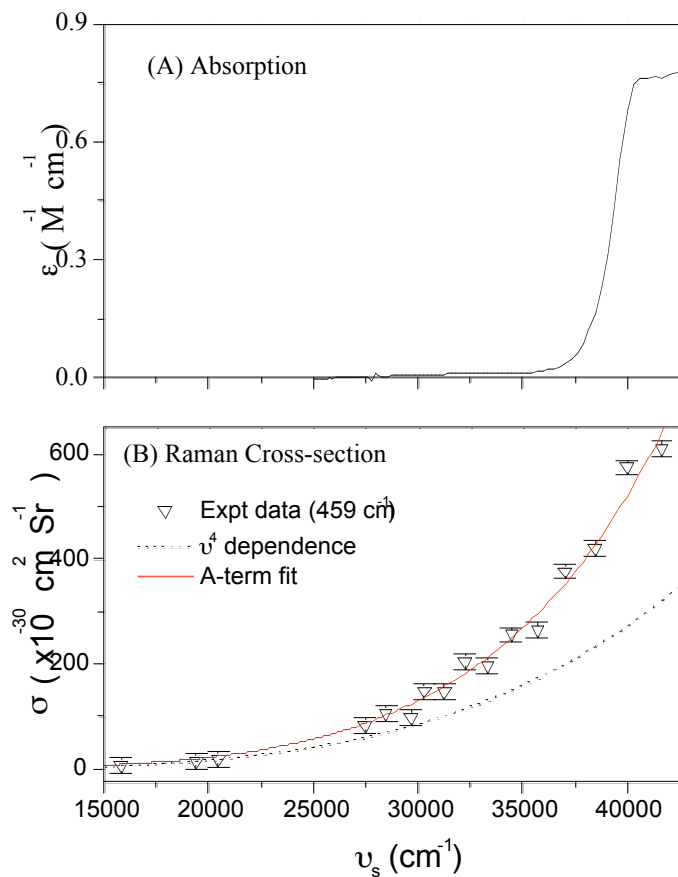


Figure 2: (A) UV absorption spectrum of CCl₄; (B) Excitation profile of ν_1 mode, CCl₄ between 635 and 240 nm. See reference 56 for experimental details.

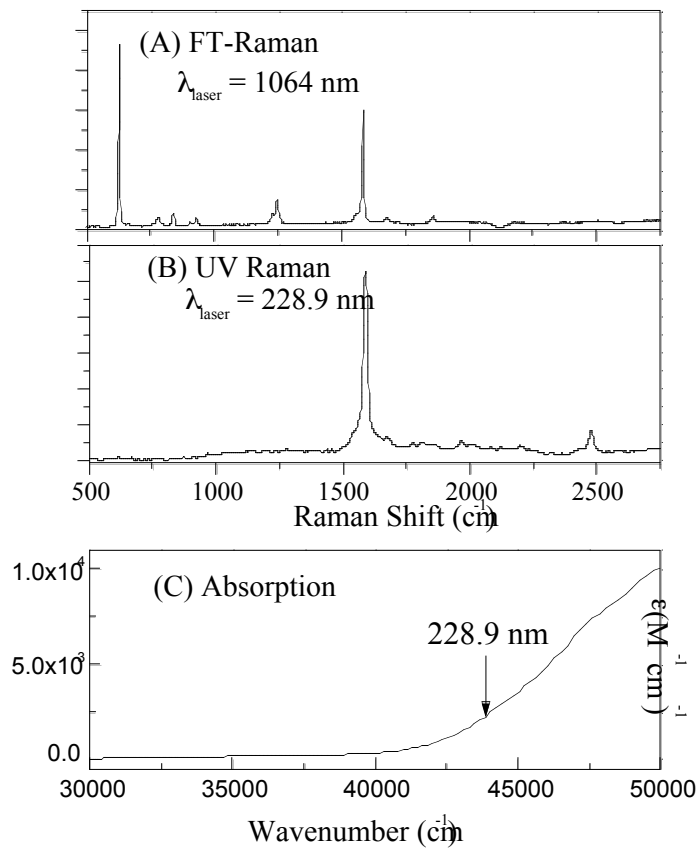


Figure 3: (A) Raman spectrum of trichloroethylene (TCE) measured by a Bruker FT-Raman system with the excitation at 1064 nm; (B) UV-Raman spectrum of TCE excited at 228.9 nm by using Coherent Frequency double Ar^+ ion laser. The cutoff of the edge filter is about 350 cm^{-1} . The SPEX 750M spectrometer (2400 lines/mm grating) and liquid N_2 cooled CCD (Princeton Instruments) were used to record the spectra. (C) UV absorption of TCE was collected by Perkin-Elmer 320 spectrophotometer.

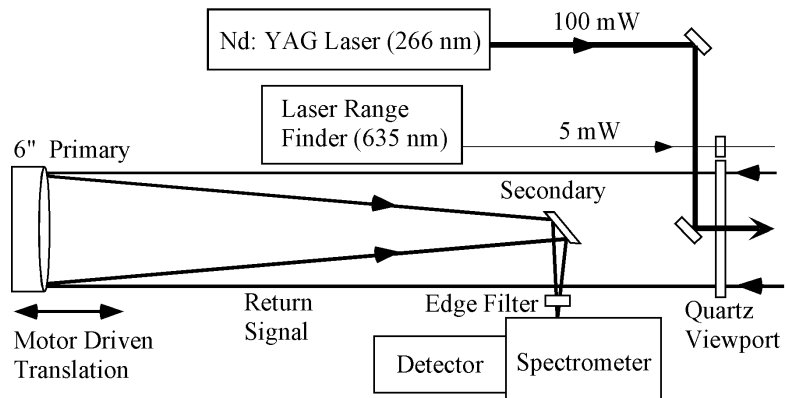


Figure 4: Schematic diagram of the Mini-Raman Lidar System (MRLS)



Figure 5. The Mini-Raman lidar System (MRLS)

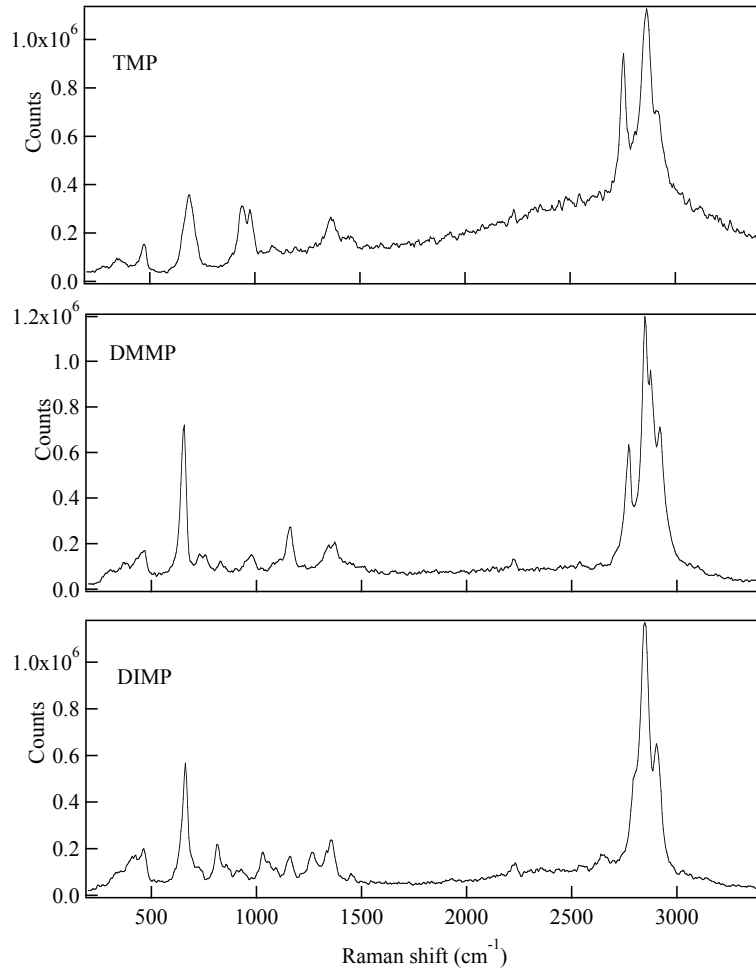


Figure 6. Raman spectrum of neat phosphate compounds at a stand-off distance of 2 meters. The vertical scale is the signal in A/D counts. The pathlength is 10 mm, and the signal integration time is 60 s for a 20 Hz Nd:YAG laser (266 nm, 100 mW average power).

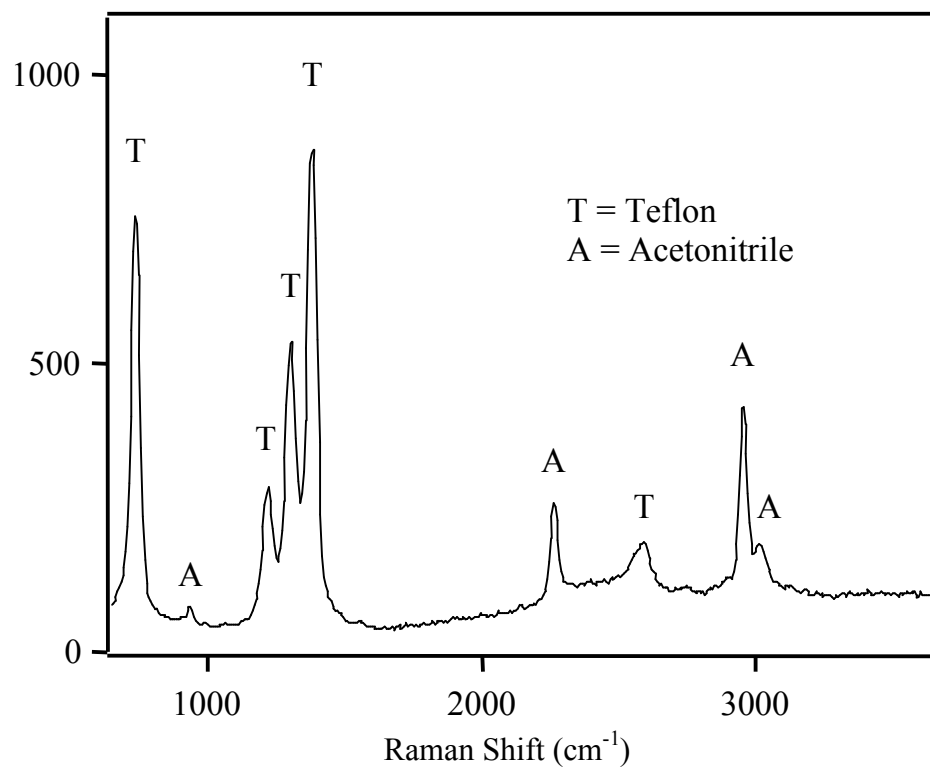


Figure 7: Raman fingerprints of a 90 μm thick film of acetonitrile on a Teflon substrate at a stand-off distance of 3 meters. Signal acquisition time is five seconds.

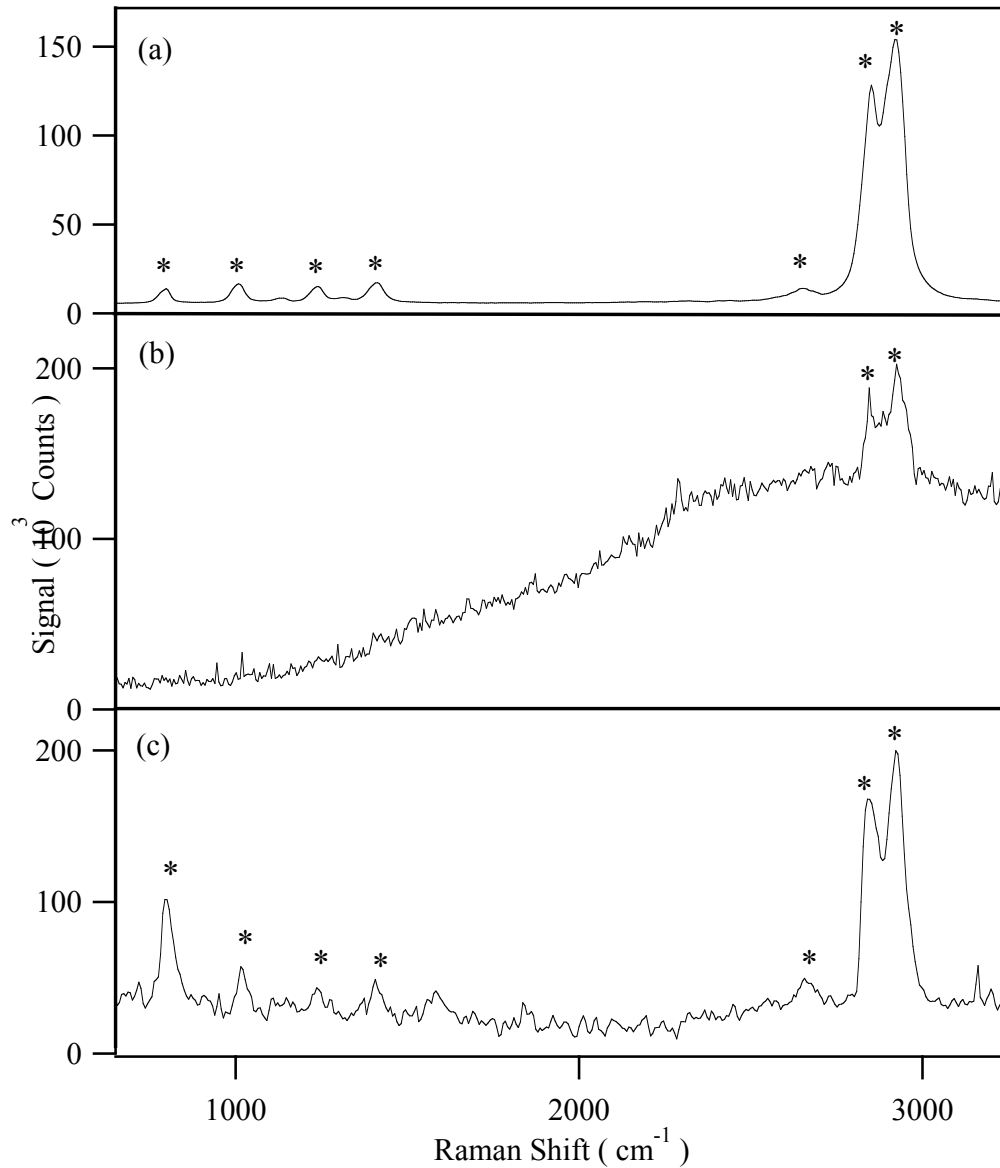


Figure 8: Raman fingerprints of cyclohexane at a stand-off distance of 2 m: (a) as a neat sample with 266 nm laser excitation; (b) on topsoil with 266 nm laser excitation; and (c) on topsoil with 248 nm laser excitation. The asterisks mark the discernible Raman features of cyclohexane. The broad background in (b) is due to fluorescence from the topsoil.

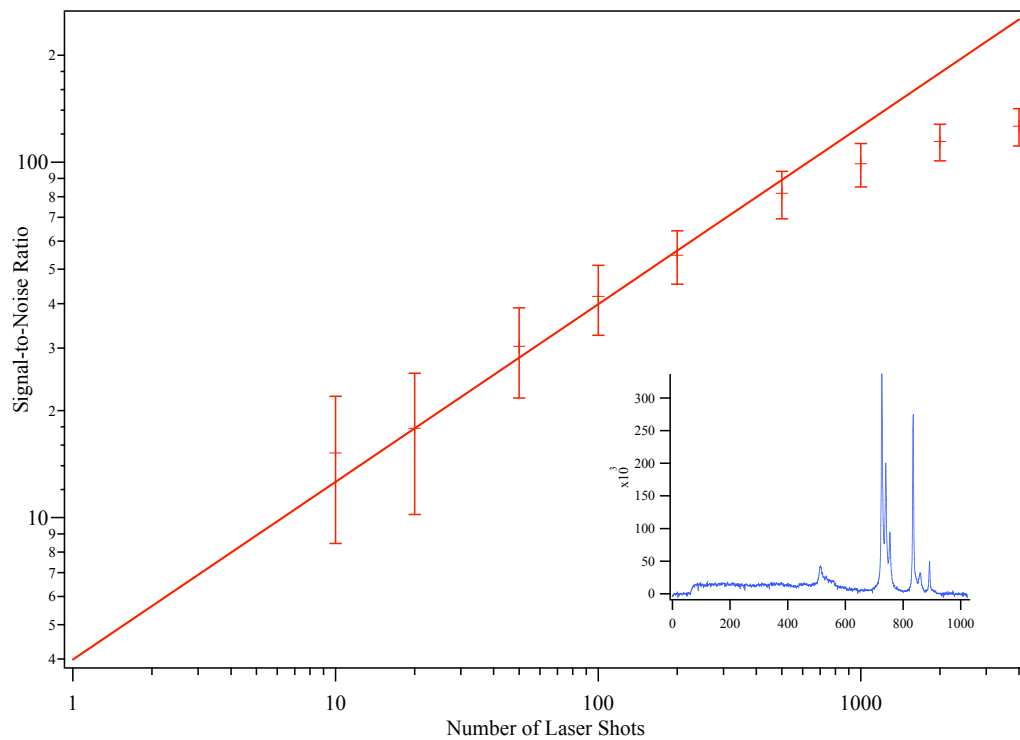


Figure 9: Log-Log plot of signal-to-noise vs. number of laser shots for the 732 cm^{-1} mode of Teflon. The straight line is the dependence in the limit that shot-noise is the only significant noise source.

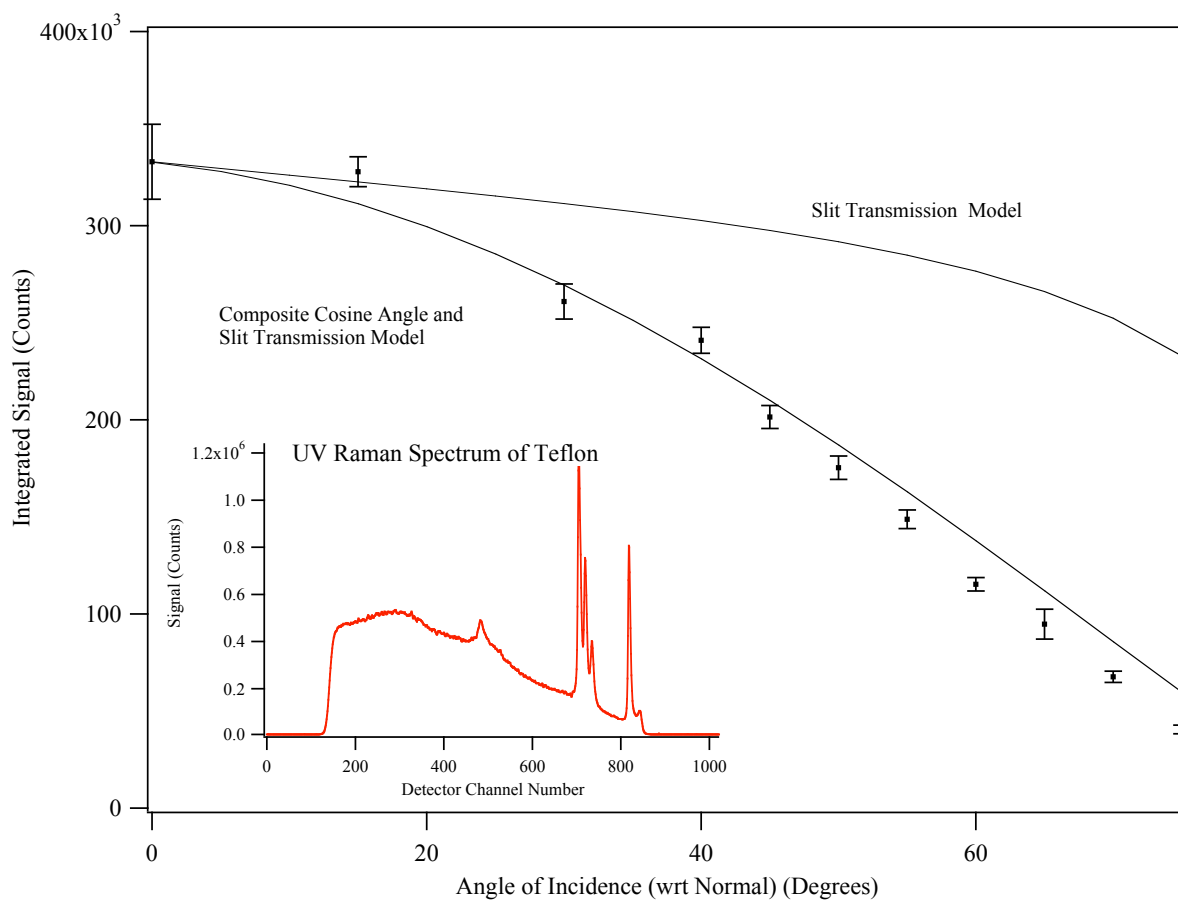


Figure 10. Total area under the 732 cm^{-1} peak of Teflon vs. angle-of-incidence between the laser beam and normal of the Teflon surface. The experimental points are shown with their associated error bars. The modeled data are shown by the solid and dashed curves.

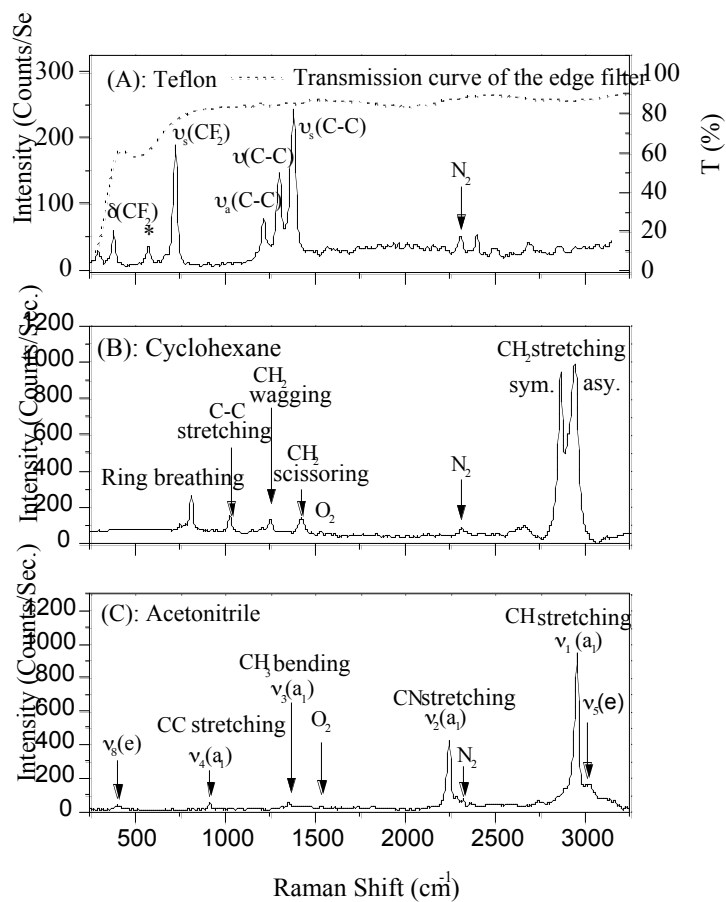


Figure 11: (A) Raman spectrum of Teflon; (B) Raman spectrum of cyclohexane; (C) Raman spectrum of acetonitrile. These spectra were measured at a distance of 533 meters by the MLRV using the 266 nm excitation (~ 8 mJ/pulse, 30 Hz) and a 16 inch collection optic. The spectra were recorded by using 100 μm slits and a 2400 line/mm grating inside a HR460 spectrograph (SPEX). The spectra were collected in 150 sec and the resolution was ~ 11 cm^{-1} . Assignments of prominent Raman features are noted. The positions of atmospheric N₂ and O₂ Raman returns are also indicated on the traces and * indicates defect structure characteristic of Teflon.

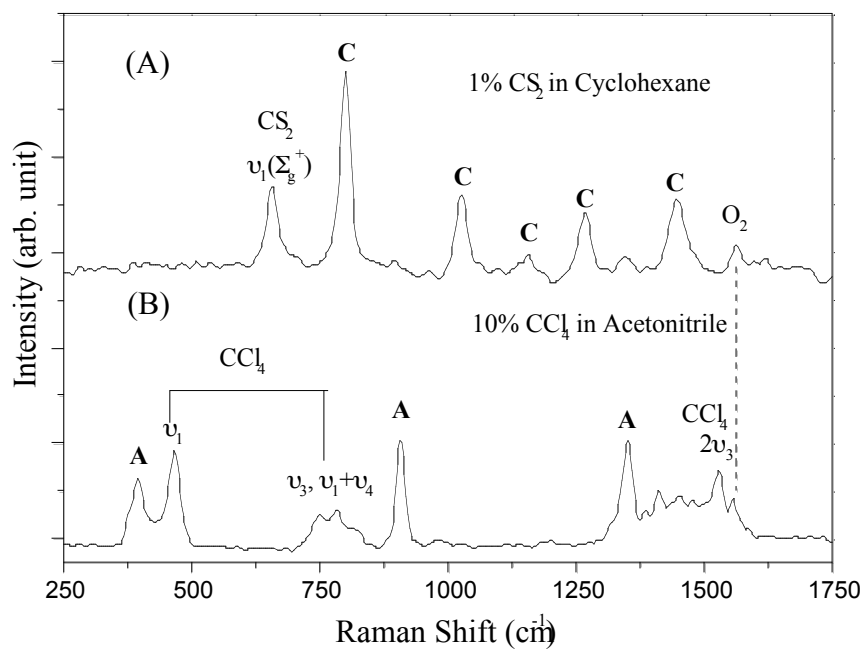


Figure 12: (A) Raman spectra of 1% (v:v) CS₂ in cyclohexane (B) Raman spectra of 10% (v:v) CCl₄ in acetonitrile collected at a range of 533 meters. The experimental conditions were the same as Figure 12. The prominent peaks from CS₂ and CCl₄ were noted. The Raman features of cyclohexane and acetonitrile were indicated as C and A respectively. Raman return from atmospheric O₂ was also marked.

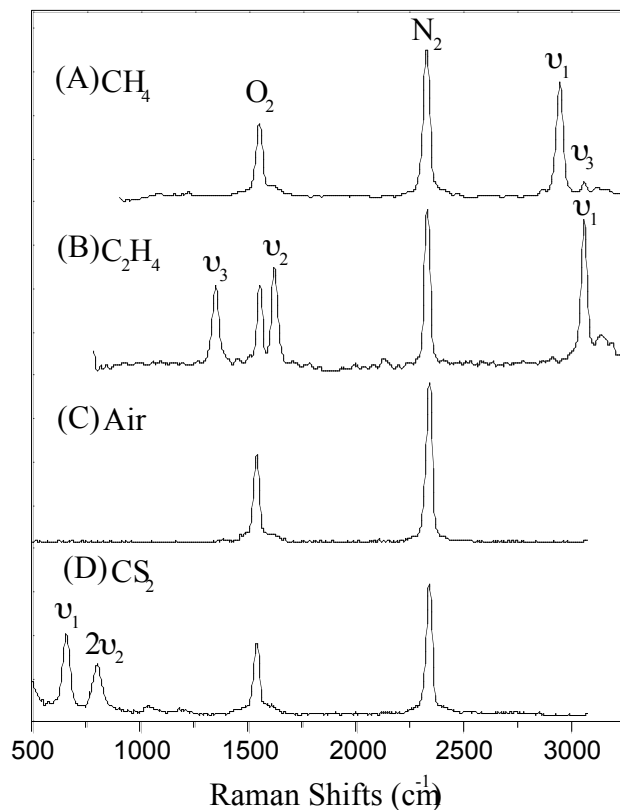


Figure 13: Raman spectra of gases were measured at a distance of 533 meter by the MLRV using the 266 nm excitation (~ 6 mJ/pulse, 30 Hz) and a 16-inch collection optic. The spectra were recorded by using 100 μ m slits and a 2400 line/mm grating inside a HR460 spectrograph (SPEX). The spectra were collected by ICCD in 90 sec and the gate width of ICCD was set at 50 ns. (A) Spectrum of 200 torr CH_4 in a 2 meter gas cell; (B) Spectrum of C_2H_4 from a 2 meter gas cell with 200 torr pressure; (C) Spectrum of air sampling over a 8 meter path length, which was determined by the gate width of the ICCD. (D) Spectrum of 30 torr CS_2 in a 2 meter gas cell. Figures of (A), (B), and (D) were an average of six single spectra that accumulated in 90 seconds, while Figure (C) was a single spectrum integrated in 90 second (2700 laser pulses).



Figure 14. Handheld Surface-Enhanced Resonance Raman Spectroscopy (SERRS) lidar.
Reprinted with permission. [70, 74]

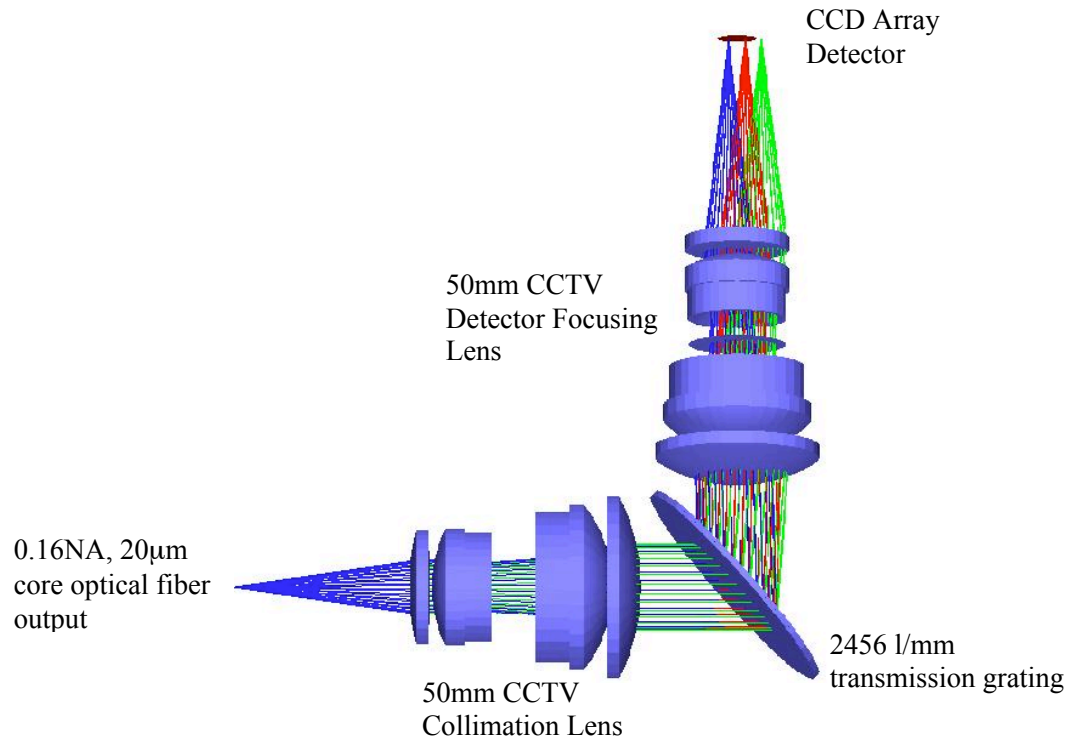
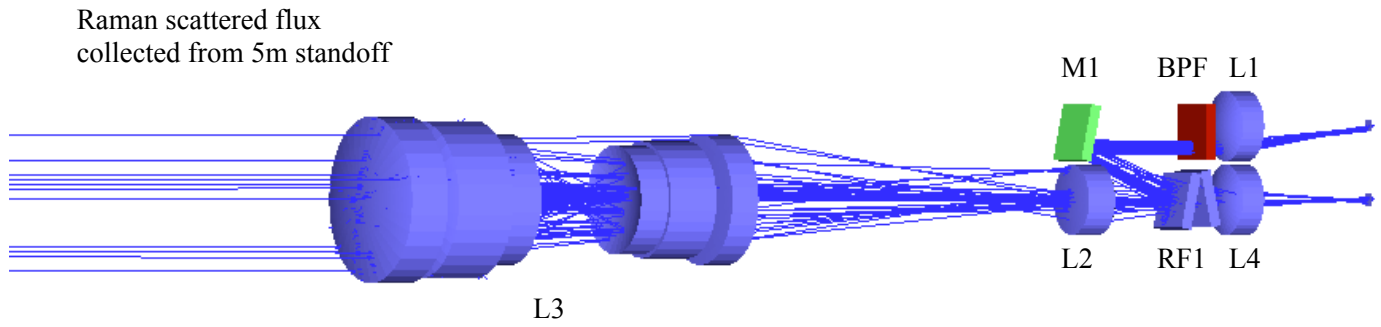


Figure 15. A. Non-sequential ray-trace of Raman probe head using Zemax 9.0. Rayleigh scattered flux reflected using long-pass filter into laser delivery optical fiber. Fiber bandpass filter shown in red. Mirror shown in green. B. Raytrace of spectrograph employing volume-phase holographic grating using Zemax 9.0. Reprinted with permission. [70, 74]

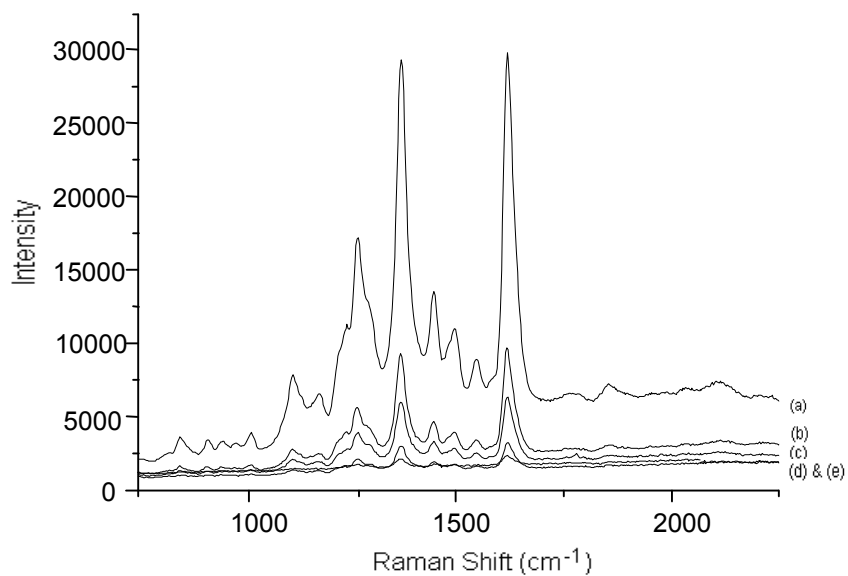


Figure 16: Taken from Reference [70]. Graph showing effect on spectral intensities of ABT DMOPA as a function of distance using a Renishaw System 100 outfitted with modified optics. The output power of the 532 excitation wavelength was 3.6mW and the collection time was 20s. The various standoff distances were: (a) 2m, (b) 3m, (c) 4m, (d) 6m, and (e) 10m.

References:

- [1] The March 1995 Tokyo subway attack involving the nerve agent sarin deployed by the Aum Shinrikyo cult.
- [2] The fall of 2001 mail attacks in the United States involving *B. Anthracis* spores.
- [3] Ray, M. D., Sedlacek, A. J., and Wu, M. 2000, *Rev. Sci. Instr.* **71**, 3485.
- [4] Wu, M., Ray, M.D., Fung, K.H., Ruckman, M. W., Harder, D. and Sedlacek, A. J. 2000, *Appl. Spectros.* **54**, 800.
- [5] Sedlacek, A. J., Ray, M. D., Higdon, N. S., Richter, D. A. 2001, *Proceedings of SPIE, Vibrational Spectroscopy-based Sensor Systems* (S. D. Christesen and A. J. Sedlacek, III, Ed.) 95.
- [6] Hoge, F. E. and Swift, R. N. 1980, *Appl. Optics* **19**, 3269; Hoge, F. E., Swift, R. N. 1981, *Appl. Optics*, **20**, 1191; Hoge, F. E. and Swift, R. N. 1981, *Appl. Optics*, **20**, 3197.
- [7] Hengstermann, T. and Reuter, R. 1990, *Appl. Optics*, **29**, 3218.
- [8] Yamagishi, S., Hitomi, K., Yamanouchi, H., Yamaguchi, Y. and Shibata, T. 2001, *SPIE Proceedings on Hyperspectral Remote Sensing of the Ocean*, Ed.: Frouin, R. J., Hiroshi, K. and Motoaki, K., **4154** 136.
- [9] Diebel, D., Hengstermann, Reuter, R., and Willkomm, R. 1989, *The Remote Sensing of Oil Slicks*, Ed. A. E. Lodge, John Wiley and Sons Ltd.,
- [10] Hoge, F. E., Swift, R. N. and Yungel, J. K. 1983, *Appl. Optics* **22**, 2991.
- [11] Moya, I., Guyot, G., and Goulas, Y. 1992, *ISPRS J. Photogramm. Remote Sensing* **47**, 205.
- [12] Grant, W. B. 1990, *Optical Eng.* 30, 40.
- [13] Measures, R. M. 1992, *Laser Remote Sensing: Fundamentals and Applications*; Krieger Publishing Co., Malabar FL.
- [14] Hinkley, E. D., 1973, *Topics in Applied Physics, Laser Monitoring of the Atmosphere* **14**, Springer-Verlag: New York.
- [15] Grant, W. B., Browell, E. V., Menzies, R. T., Sassen, K. and She, C-Y 1997, *SPIE Milestone Series, Laser Applications in Remote Sensing*, 141.
- [16] Reichardt, J., Wandinger, U., Serwazi, M and Weitkamp, C. 1996, *Opt. Eng.* **35**, 1457.
- [17] Ansmann, A., Riebesell, M., Wandinger, U., Weitkamp, C., Voss, E., Lahmann, W. and Michaelis, W. 1992, *Appl. Phys. B: Photophys. Laser Chem.* 55, 18.
- [18] Turner, D. D., and Goldsmith, J.E.M. 1999, *J. Atmos. Oceanic Technol.*, **16**, 1062.
- [19] Turner, D. D., Feltz, W.F. and Ferrare, R.A. 2000, *Bull. Amer. Meteor. Soc.*, **81**, 1301.
- [20] Harms, J., *Appl. Optics*. 18, 1559 (1979); Harms, J., Lahmann, W. and Weirkaml, C. 1978, *Appl. Optics*, 18, 1559.
- [21] Milton, M. J. T., Woods, P. T., Jolliffe, B. W., Swann, N. R. W. and McIlveen, T. J. 1992, *Appl. Phys. B* **55**, 41.
- [22] Rothe, K. W., Brinkmann, U. and Walther, H. 1974, *Appl. Opt.* 4, 181.
- [23] Oh, C., Prasad, C. R., Fromzel, V., Hwang, I. H., Reagan, J. A., Fang, H. and Rubio, M. 1999, *Proceedings of the SPIE Conference on Laser Radar Technology 3707*, 17186.
- [24] Edner, H., 1995, *Review of Laser Engineering* 23, 142.
- [25] Edner, H., Faris, G. W., Sunesson, A. and Svanberg, S. 1989, *Appl. Opt.* 28, 921.
- [26] Chyba, T. H., Zenker, J. T., McCray, C. L., Lee, H. R., Elivert, R., Thomas, B., Toppin, C., Larson, D., Higdon, N. S. and Ritcher, D. A. 1999, *SPIE Proceedings 3757*, 80.
- [27] Sunesson, J. A., Apituley, A. and Swart, D. P. J. 1993, *Appl. Opt.* 33, 7045.
- [28] Papayannis, A., Ancellet, G., Pelon, J. and Megie, G. 1989, *Appl. Opt.* 29, 467.
- [29] Sedlacek, A. J., Harder, D., Leung, K.P., Zuhoski, P.B., Burr, D. and Chen, C. L. 1995, *Remote Sensing of the Atmosphere by Resonance Raman LIDAR*, Sixth Optical Remote Sensing of the Atmosphere, Salt Lake City, UT, February 6.
- [30] Leonard, D. A. 1976, *Nature* 216, 142.
- [31] Cooney, J. A. 1968, *Appl. Phys. Lett.* 12, 40.
- [32] Melfi, S. H., 1972, *Appl. Opt.* 11, 1605.

-
- [33] Inaba, H. and Kobayasi, T. 1968, *Nature* 224, 170; 1970, *Appl. Phys. Lett.*, 17, 139; 1972, *Opto-Electronics* 4, 101.
- [34] Bilbe, R.M., Bullman, S.J. and Swaffield, F. 1990, *Meas. Sci. Technol.* 1, 495.
- [35] Inaba, H., 1976, *Laser Monitoring of the Atmosphere* E. D. Hinkley (Ed.), Springer-Verlag, New York.
- [36] Houston, J.D., Sizgoric, S., Ulitsky, A. and Banic, J. 1986, *Appl. Optics* 25, 2115.
- [37] Sedlacek, A. J., Harder, D., Leung, K.P., Zuhoski, P.B., Burr, D. and Chen, C. L. 1995, *Remote Sensing of the Atmosphere by Resonance Raman LIDAR*, Sixth Optical Remote Sensing of the Atmosphere, Salt Lake City, UT, February 6. 1995
- [38] Ahmad S. R. and Billiet E. M. 1991, *Optics and Laser Technology* 23, 128.
- [39] Renaut, D. and Capitini, R. 1980, *J. Atmos. Oceanic Tech.* 5, 585.
- [40] Renaut, D., Pourney, J. C. and Capitini, R. 1980, *Optics Lett.* 5, 233.
- [41] Balsiger, F. and Philbrick, C. R. 1996, *Application of Lidar to Current Atmospheric Topics*, SPIE Proceedings 2833, 231.
- [42] Philbrick, C. R. 1994, *Lidar Measurements of Water Vapor Concentrations in the Troposphere*, IEEE, 2043.
- [43] Cooney, J. A. 1986, *Appl. Opt.* 25, 2035.
- [44] Cooney, J. A. 1987, *Appl. Opt.* 26, 3487.
- [45] Raman, C. V. Krishnan, K. S. 1928, *Nature*, 121(3048) 501.
- [46] Kryskowski, D. and Suits, G. H., Chapter 3 1993, *The Infrared & Electro-Optical Systems Handbook – Sources of Radiation*, Editor: George J. Zissis, SPIE Optical Engineering Press and Infrared Information Analysis Center copublishers.
- [47] Weber, A. (Ed) 1979 *Raman Spectroscopy of Gases and Liquids*, Springer-Verlag, Berlin.
- [48] Ziegler, L. D., and Hudson, B. 1981, *J. Phys. Chem.* 74, 982. and Ziegler, L. D., and Hudson, 1983, *J. Chem. Phys.*, 79, 1134; Mayne, L. C., Ziegler, L. D., and Hudson, B. 1985, *J. Phys. Chem.* 89, 3395; Harhay, G. P., and Hudson, B. S. 1993, *J. Phys. Chem.* 97, 8158; Gerrity, D. P., Ziegler, L. D., Kelly, P. B., Desiderio, R. A., and Hudson, B. 1985, *J. Chem. Phys.* 83, 3209.
- [49] Rava, R. P., and Spiro, T. G. 1984, *J. Am. Chem. Soc.* 106, 4062; Rava, R. P., and Spiro, T. G. 1985, *J. Phys. Chem.* 89, 1856; Caswell, D., and Spiro, T. G. 1986, *J. Am. Chem. Soc.* 108, 6470.
- [50] Johnson, C. R., Ludwig, M., O'Donnell, S. E., and Asher, S. A., 1984, *J. Am. Chem. Soc.* 106, 5008; Asher, S. A., and Johnson, C. R., 1985, *J. Phys. Chem.* 89, 1375; Johnson, C. R., Ludwig, M., and Asher, S. A., 1986, *J. Am. Chem. Soc.* 108, 905; Asher, S. A., Ludwig, M., and Johnson, C. R., 1986, *J. Am. Chem. Soc.* 108, 3186; Asher, S. A., and Murtaugh, J. L. 1988, *Appl. Spectros.* 42, 83; Harmon, P. A., and Asher, S. A. 1990, *J. Chem. Phys.* 93, 3094.
- [51] Li, B., and Myers, A. B. 1990, *J. Phys. Chem.* 94, 4051; Phillips, D. L., and Myers, A. B. 1991, *J. Chem. Phys.* 95, 226; Makel, F., and Myers, A. B. 1993, *J. Chem. Phys.* 98, 21; Myers, A. B., Li, B., and Ci, X. 1988, *J. Chem., Phys.*, 89, 1876; Myers, A. B., and Li, B. 1989, *J. Chem. Phys.*, 92, 3310
- [52] Turlson, M. O., and Mathies, R. A. 1986, *J. Chem. Phys.* 84, 2068.
- [53] Schomacker, K. T., Delaney, J. K., and Champion, P. M. 1985, *J. Chem. Phys.* 85, 4240.
- [54] Ohwada, K., Takahashi, A., and Fujisawa, G. 1995, *Appl. Spectros.*, 49, 216.; Ohwada, K., Takahashi, A., and Fujisawa, G. 1996, *Spectro. Acta. A*, 52, 149.
- [55] Ahmad, S. R., and Foster, V. G. 1998, *Appl. Spectros.*, 52, 70; Ahmad, S. R. and Foster, V. G. 2000, *J. Raman Spectros.* 31, 1023.
- [56] Wu, M., Ray, M. and Sedlacek, A. J. 1998, *J. Chem. Phys.*, 109, 1352.
- [57] Long, D. A. 1977, *Raman Spectroscopy*, McGraw-Hill Inc., New York.
- [58] Spiro, T. S. 1987, *Biological Application of Raman Spectroscopy*, John Wiley & Sons, New York;
- [59] Asher, S. A. 1993, *Anal. Chem.*, 65, 201A; Asher, S. A. 1988, *Ann. Rev. Phys. Chem.*, 39, 537; Asher, S. A. 1993, *Anal. Chem.*, 65, 59A
- [60] Weber, A. 1979 “Raman Spectroscopy of Gases and Liquids”, Springer-Verlag, New York, page 140.
- [61] Dudik, J. M., Johnson, C. R., and Asher, S. A. 1985, *J. Phys. Chem.* 89, 3805.

-
- [62] Robin, M. B., 1985, "Higher Excited States of Polyatomic Molecules, Vol. 3, p209, Academic Press, Inc., New York.
- [63] Angel, S. M, Kulp, T. F., and Vess, T. M., 1992, *Appl. Spectros.* 46, 1085.
- [64] Bower, D. I. and Maddans, W. F. 1988, *The Vibrational Spectroscopy of polymers*, Cambridge University Press, Cambridge.
- [65] Chappelle, W., Wood, F. M., McCurtey, J. E. and Newcomb, W. W. 1984, *Applied Optics* 23, 134.
- [66] Dr. Chris Dyer, Defence Science and Technology Laboratory (DSTL)/UK, private communication.
- [67] Higdon, N. S., Chyba, T. H., Richter, D. A., Ponsardin, P.L., Armstrong, W.T., Lobb, C. T., Kelly, B. P. and Sedlacek, A. J. 2001, *Laser Interrogation of Surface Agents (LISA) for Military Sensing Missions*, Fifth Joint Conference on Standoff Detection for Chemical and Biological Defense, Williamsburg, VI, September, 24-28, 2001.
- [68] Becket, C. W., Pitzer, K. S. and Spitzer, R. 1967, *J. Am. Chem. Soc.* 69, 2488.
- [69] Herzberg, G. 1945, *Molecular Spectra and Molecular Structure II. Infrared and Raman Spectra of Polyatomic Molecules*, Van Nostrand Reinhold, New York.
- [70] McCabe, A., Smith, W. E., Thomson, G., Bachelder, D., Ashcroft, G and Foulger, B. F., *Appl. Spectros. In press.*
- [71] Vo-Dinh, T. 1998, *Trend Anal. Chem.* **17** 557.
- [72] Zou, S.; Williams, C. T.; Chen, E K.-Y.; Weaver, M. J. 1998, *J. Am. Chem. Soc.* **120**, 3811; Zou, S.; Weaver, M. J.; Li, X. Q.; Ren, B.; Tian, Z. Q. 1999, *J. Phys. Chem. B* **103** 4218; Williams, C. T.; Chan, H. Y. H.; Tolia, A. A.; Weaver, M. J.; Takoudis, C. G. 1998, *Eng. Chem. Res.* **37** 2307; Williams, C. T.; Chen, E. K.-Y.; Takoudis, C. G.; Weaver, M. J. 1998, *J. Phys. Chem. B* **102** 4785; Williams, C. T.; Takoudis, C. G.; Weaver, M. J. 1998, *J. Phys. Chem. B* **102** 406; Williams, C. T.; Tolia, A. A.; Chan, H. Y. H.; Takoudis, C. G.; Weaver, M. J. 1996, *Catalysis.* **163** 63; Williams, C. T.; Tolia, A. A.; Weaver, M. J. 1996, *Chem. Eng. Sci.* **51** 1673.
- [73] Wang, A., Haskin, L. A. and Cortez, E. 1998, *Appl. Spectros.* 52, 477.
- [74] G. Thomson, Private Communications.